Distribution Agreement

In presenting this thesis or dissertation as a partial fulfillment of the requirements for an advanced degree from Emory University, I hereby grant to Emory University and its agents the non-exclusive license to archive, make accessible, and display my thesis or dissertation in whole or in part in all forms of media, now or hereafter known, including display on the world wide web. I understand that I may select some access restrictions as part of the online submission of this thesis or dissertation. I retain all ownership rights to the copyright of the thesis or dissertation. I also retain the right to use in future works (such as articles or books) all or part of this thesis or dissertation.

Signature:

_____ _____

Xin Du Date

Experimental and Computational Research on
Cooperative Rearrangement in Glassy Systems
By

Xin Du
PhD

Physics

Eric Weeks
Advisor

Stefan Boettcher
Committee Member

Connie Roth
Committee Member

Kurt Warncke
Committee Member

Sven Behrens
Committee Member

Accepted:

Lisa A. Tedesco, Ph.D.
Dean of the James T. Laney School of Graduate Studies

Date

Experimental and Computational Research on Cooperative Rearrangement in Glassy Systems

By

Xin Du

B.Sc., Nanjing University, China, 2010

Advisor: Eric Richard Weeks, PhD.

An abstract of

A dissertation submitted to the Faculty of the

James T. Laney School of Graduate Studies of Emory University

in partial fulfillment of the requirements for the degree of

Doctor of Philosophy

in Physics

Summer, 2016

Abstract

Experimental and Computational Research on Cooperative Rearrangement in Glassy Systems

By Xin Du

The study of the dynamics properties of the soft materials approaching jamming transition is very important for understanding the universal mechanism underlying the jamming transition. In this dissertation, we study the jamming transition from two aspects: the correlation between the cooperative dynamics of jamming system with the free energy landscape of the system and the correlation between the dynamic properties with the structural heterogeneity of the system.

In the simulation project, we study the free energy landscape of a simple model possessing some qualitative features of glass transition. The model consists of three soft Brownian disks confined in a circular confinement, in which there are two energy local minima and one transition state. The two energy local minima corresponds to two inherent structures and the transition between the local minima involves cooperative rearrangement of the disks. If the circular region is large, the disks freely rearrange, but rearrangements are rarer for smaller system sizes. We directly measure a one-dimensional free energy landscape characterizing the dynamics. This landscape has two local minima, separated by a free energy barrier which governs the rearrangement rate. We study several different interaction potentials and demonstrate that the free energy barrier is composed of a potential energy barrier and an entropic barrier. The heights of both of these barriers depend on temperature and system size,

demonstrating how non-Arrhenius behavior can arise close to the glass transition.

In experimental project, we study the jamming of a slowly evaporating quasi two-dimensional emulsion system. In this system, water slowly evaporates from an open edge of the chamber and, as a consequence, the packing fraction of oil droplets gradually increases. By means of microscopy, we track the dynamics of droplets and identify the droplet's outlines and geometric properties. By qualifying the structural heterogeneity based on the Voronoi Vector field [1], we find the correlation between the geometric response and mechanical response to the slow increase of packing fraction.

Experimental and Computational Research on Cooperative Rearrangement in Glassy Systems

By

Xin Du
B.Sc., Nanjing University, China, 2010

Advisor: Eric Richard Weeks, PhD.

A dissertation submitted to the Faculty of the
James T. Laney School of Graduate Studies of Emory University
in partial fulfillment of the requirements for the degree of
Doctor of Philosophy
in Physics

Summer, 2016

Contents

List of Figures

Acknowledgments

Firstly, I would like to express my sincere gratitude to my advisor Prof. Eric Weeks for his support on my PhD research with his patience, kindness, a sense of humor, optimism, and immense knowledge. His guidance helped me in all the time of research and writing of this thesis. I could not have imagined having a better advisor and mentor for my Ph.D study. Without Prof. Weeks as a role model of a wonderful professor working with me for six years, I would never have the courage to pursue a career in academia.

Besides my advisor, I would like to thank the rest of my thesis committee members, Prof. Stefan Boettcher, Prof. Connie Roth, Prof. Kurt Warncke and Prof. Sven Behrens, for their insightful comments and encouragement, but also for the hard question which incented me to widen my research from various perspectives. Thanks to Prof. Stefan Boettcher for his support on my job searching and for his great mentoring as my advisor for my second rotation project which stimulates my interest in computational physics research. Thanks to Prof. Connie Roth for her advice and support on my research during my Ph.D study. And thanks to Prof. Kurt Warncke for having the casual and warm conversations with me during my first year at Emory, which is very helpful for me to get involved in the warm family in physics department.

I would like thank my fellow labmates, Dandan Chen, Kazem Edmond, Gary Hunter, Ken Desmond, Carlos Orellana, Xia Hong, Skanda Vivek, Cong Cao for the stimulating discussions and for all the fun in both life and academia we have had during the past few years. Special thanks to Gary Hunter for his support on the simulation project (Chap. 2) and special thanks to Carlos Orellana for his support on the experimental project on 2-D emulsions (Chap. 4).

Xin Du

Emory University

Summer 2016

Chapter 1

Introduction

1.1 Soft Material

Soft materials are defined as the materials that have both solid-like properties and liquid-like properties. They are commonly seen in our everyday life, for example, tooth paste, ink, blood, sand, and shaving foam. Figure 1.1 shows some examples of soft materials in real life including grains, toothpaste, mayonnaise and shaving cream. What is the physics behind the process of glass blowing? Why can peanut butter be spread on bread like a liquid, but it does not flow when you flip the bread over? Why can one quickly run across a pool filled with corn starch and water, but sinks when stand on the suspension? These questions are the key to soft matter physics: the study of materials with both solid-like and fluid-like properties. My graduate study focuses on answering those questions by relating the macroscopic properties with the microscopic structures.

In physics laboratory, scientists study a variety types of soft materials, including

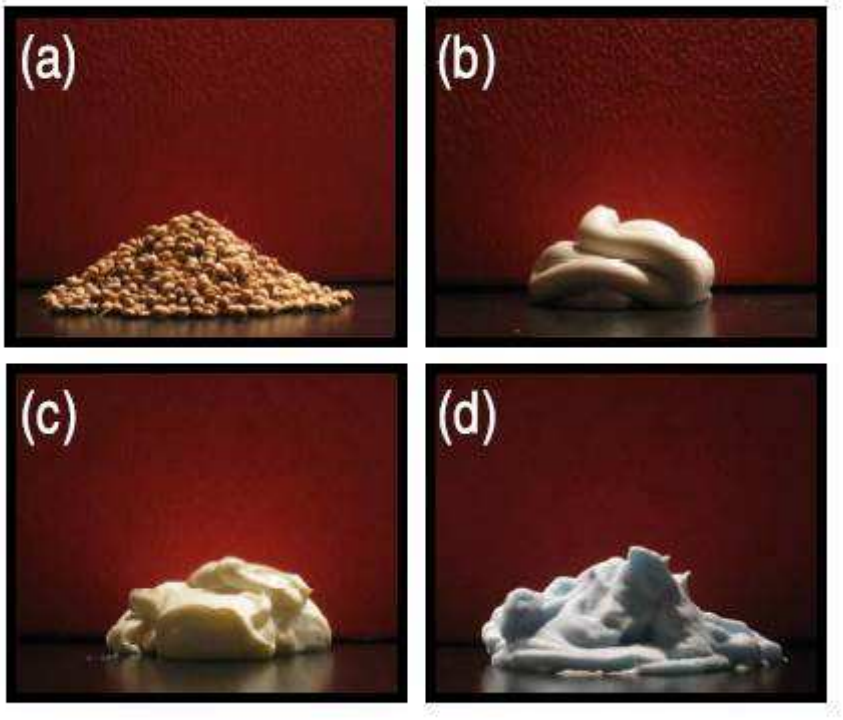

Figure 1.1: Examples for soft materials in everyday life. (a) Granular media, consisting of solid grains in gas or vacuum. (b) Toothpaste, a dense packing of (colloidal) particles in fluid. (c) Mayonnaise, an emulsion consisting of a dense packing of (oil) droplets in an immiscible fluid. (d) Shaving foam, a dense packing of gas bubbles in fluid. Adapted from [2] with permission by IOP Publishing. Link: http://iopscience.iop.org/article/10.1088/0953-8984/22/3/033101?fromSearchPage=true

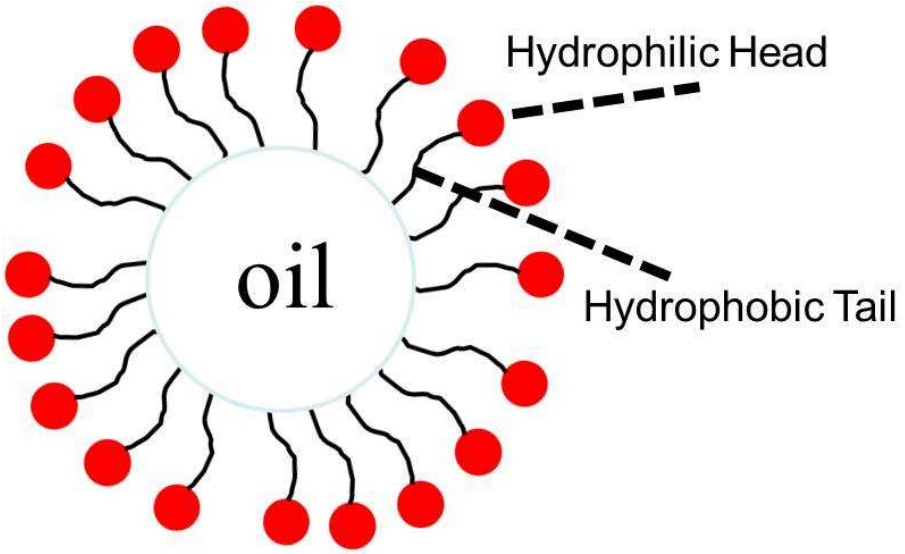

Figure 1.2: (Color online) Sketch of an emulsion droplet stabilized by surfactant molecules. Not to scale: typically the surfactants are tiny molecules, whereas the droplet is in micron size.

colloidal suspensions, emulsions, foams, gels, and granular materials. A colloidal suspension is a heterogeneous system with solid particles in dimensions of order $10\mu m$ or less dispersed in a liquid medium [3]. Toothpaste in Fig. 1.1(b) is an example of colloidal suspensions. Emulsions consist of liquid droplets that are stabilized by surfactant molecules, mixed into another kind of immiscible liquid. Mayonnaise in Fig. 1.1(c) is a emulsion system. Foams, like shaving foam in Fig. 1.1(d), are gas bubbles dispersed in liquid. Gels are collections of particles (such as colloidal particles) that are stuck together due to the attractive interactions. Granular materials are the materials composed of discrete, large ($> 100\mu m$ in diameter) solid particles (often called grains). Figure 1.1(a) is a good example for granular materials. One common feature shared by these materials is that they are typically mixtures composed of two or more materials.

My graduate research focuses on studying the properties of two dimensional emulsions. As is shown in Fig. 1.2, surfactant molecules embrace the droplet and keep it in a spherical shape. Surfactant molecules have a hydrophilic head that prefers to stay with water phase and a hydrophobic tail that prefers oil phase. Due to surface tension, the droplets in an emulsion are stabilized by the surfactant molecule as a spherical shape which minimizes surface area and the cost of surface energy. Since the surfactant can lower the surface energy, the emulsion droplets are very soft and largely deformable. When they are packed closely together, they contact with neighbor droplets and deform into irregular shapes. Microfluidic techniques can precisely produce droplets with sizes in a wide range from micrometer to millimeter [3]. The packing fraction of emulsions widely ranges from 0 to 1. Emulsions are a great model for studying the properties of soft materials because they have three features: (1) it is straightforward to generate controllable uniform sized emulsion droplets employing microfluidics techniques; (2) the emulsion droplets are easily deformable, which introduces measurable force chains among the droplets; (3) the emulsions are made from silicon oil or mineral oil and water, which is inexpensive. In this dissertation, chapter 4 provides a detailed discussion about the dynamics of a slowly compressed quasi-2D emulsion system.

1.2 Jamming Transition

In 1998 Liu and Nagel noted that there are many soft materials with solid-like properties, and they suggested that perhaps all of these become solid-like by some universal process, a jamming transition [4]. They proposed a phase diagram for

jamming with three control parameters, volume fraction, shear stress and temperature as is shown in Fig. 1.3. (1) In many of soft materials like emulsions and foams, the transition is seen as the volume fraction of droplets or particles is increased. For example, shaving foam with bubbles gets jammed if some of the liquid evaporates. (2) A jammed material is structurally disordered and possesses a yield stress. If an applied stress exceeds the yield stress, the material flows, like peanut butter can be spread onto bread. (3) In window glass, the jamming transition is the glass transition as the temperature is decreased. The key idea of jamming is that all of these transitions from liquid-like to solid-like may be due to a universal underlying physics [5].

To understand the universality of the jamming transition, scientists have been studying the scaling law of some material properties, including structural, dynamics and mechanical properties, as the system approaches jamming transition. If a particular scaling law is consistent for different soft materials, then it would suggest that this relationship is governed by a universal mechanism underlying the jamming transition [7, 8] There are several examples of possible universal scaling. For instance, below the jamming transition ($\phi < \phi_c$), the particles in colloidal suspensions could rearrange on some typical time scale τ, and as the colloidal suspensions approaching jamming transition, the time scale τ diverges when the rearrangements hardly occur [9–13]. In Chap. 2, we will introduce a computational research on the time scale of the rearrangement in a jamming system.

In Chap. 4, we study the jamming of soft/deformable particles, emulsion droplets, which interact through repulsive contact force. With more deformation, the droplets are more close to jamming transition. And the amount of deformation of the droplets

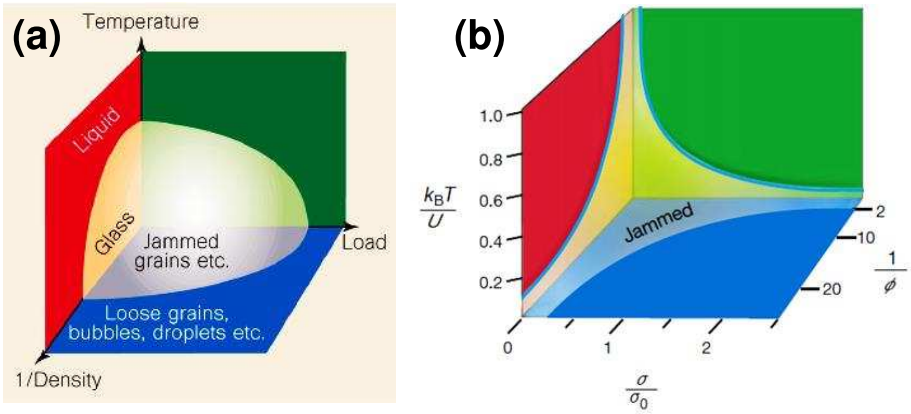

Figure 1.3: Jamming phase diagrams. (a) The control parameters are temperature, 1/density, and applied load. The states which lie within the curved surface, close to the origin, are jammed states. The red plane formed by temperature and 1/density is the regular glass transition, where the inverse density represents the influence of the more normal glass transition parameter pressure. As temperature increase or density gets smaller, it becomes liquid. For grains, bubbles, droplets, etc, the inverse density is equivalent to inverse volume fraction, or inverse area fraction if 2D. If the load is above the yield stress, the materials unjam and flow like liquids. Crossing the jamming transition surface make the material transit from unjammed state to jammed state, or vice versa.(b) Jamming phase diagram for attractive particles. The control parameters are the ratio between thermal energy k_BT and potential energy U due to the attraction interaction between particles: k_BT/U, inverse density: $1/\phi$ and stress σ/σ_0. It is the same that athermal system like grains, bubbles, droplets, etc sit on the blue plane formed by inverse density and applied load. (Thanks to Nature Publishing Group's permission. (a) Reprinted by permission from Macmillan Publishers Ltd: Nature ([4]), copyright (1998). License Number: . (b) Reprinted by permission from Macmillan Publishers Ltd: Nature [6], copyright (2001). License Number: 3961410262775.)

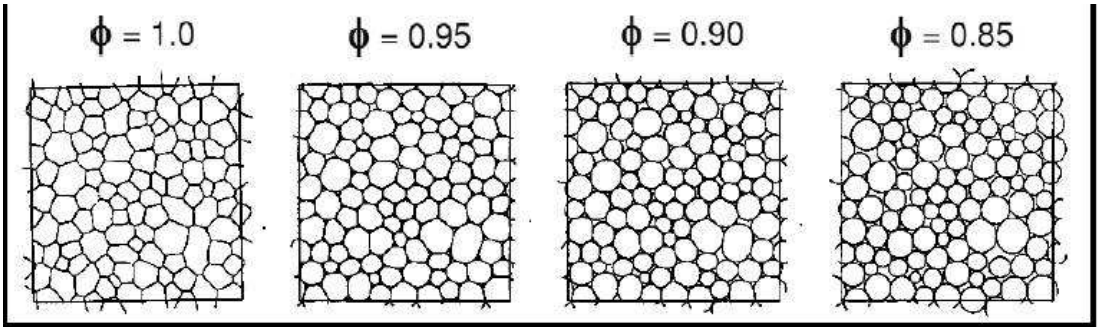

Figure 1.4: Simulated foams which loss rigidity by increasing wetness. The packing fraction, ϕ, decreases from 1.0 to 0.85 during this unjamming process. Adapted from [14] with permission. License Number: 3901030954339.)

can be controlled by enforced packing fraction. As this system approaches the rigid state, it exhibits rich interesting behavior, where geometric and mechanical response is intricately correlated [2]. In our experiment, we increase the packing fraction of binary-sized emulsions by decreasing the volume of water. This approach was applied reversely to foam system in 1990s proposed by Bolton [14]. Figure 1.4 shows the unjamming process of a simulated foam system by increases wetness [14]. When the wetness increases and packing fraction, ϕ, is lowered, the gas bubbles transform from polygons to spherical shape and the contact length between bubbles decreases. For emulsions consisting of oil droplets dispersed in water, we decrease the wetness when the water slowly evaporates. In Chap. 4, we relate the geometric response and mechanical response to the increase of packing fraction in a emulsion system.

1.3 The Energy Landscapes of Glassy System

During the last several decades, the studies on the glass transition has amazingly developed by intensive theoretical and experimental research[15–18]. Among several

perspectives for understanding glass transition, the energy landscape paradigm provides a unified understanding of glass transition. In 1969, Goldstein was the first to make the connection between the behavior of glass formers at low temperature and the potential energy landscape: the dynamics behavior of glassy system at low temperature is dominated by the local minima or basins which are separated by potential energy barriers [19]. From the view of a potential energy landscape: the state of a system of N particles can be described as the potential energy function $V(\vec{r}_1, \cdots, \vec{r}_N)$ in a $(3N+1)$-dimensional configuration space. The evolution of the system can be considered as the motion of a state point in the $(3N+1)$-dimensional configuration space along the potential energy surface. Figure 1.5 is a sketch of potential energy landscape in one-dimensional configuration space [20]. There are local minima, or basins, that are separated by local energy barriers. At low temperatures, the system is close to the local minima separated by barriers which are large relative to $k_B T$. And each local minimum corresponds to one metastable amorphous state. One important feature of the potential energy landscape proposed by Goldstein is that it only depends on the atomic coordinates and is temperature independent.

More than a decade after the Goldstein work, Stillinger and Weber further developed the concept of 'inherent structure' and represented a thermodynamic description of glass transition based on the topology of potential energy landscape [22]. Inherent structure is a term that is interchangeable with 'local minimum' and 'basin'. The configurations of a many-body system can be uniquely mapped on inherent structures by minimizing the potential energy along the steepest decent path or by the conjugate gradient algorithm. The temporal evolution of a system can be thought

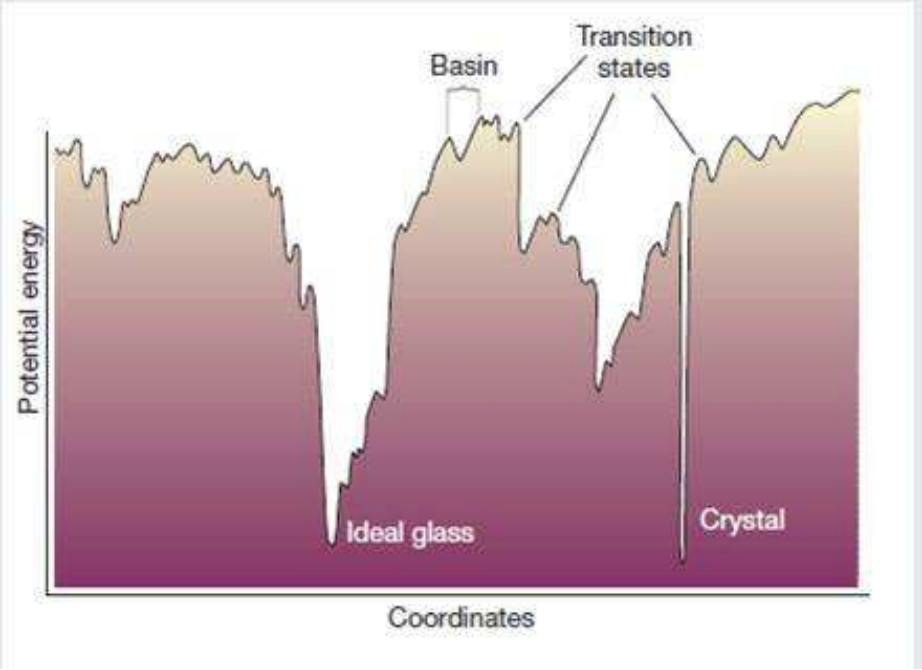

Figure 1.5: Schematic representation of the potential energy landscape. The horizontal axis represents the configurational degree of freedom, i.e. $3N$ spatial coordinates. This landscape is more reminiscent of a glass former, since a randomly chosen coordinate on the x-axis is more likely to correspond to a metastable amorphous state. Reprint with permission from [20]. License Number: 396140423614.

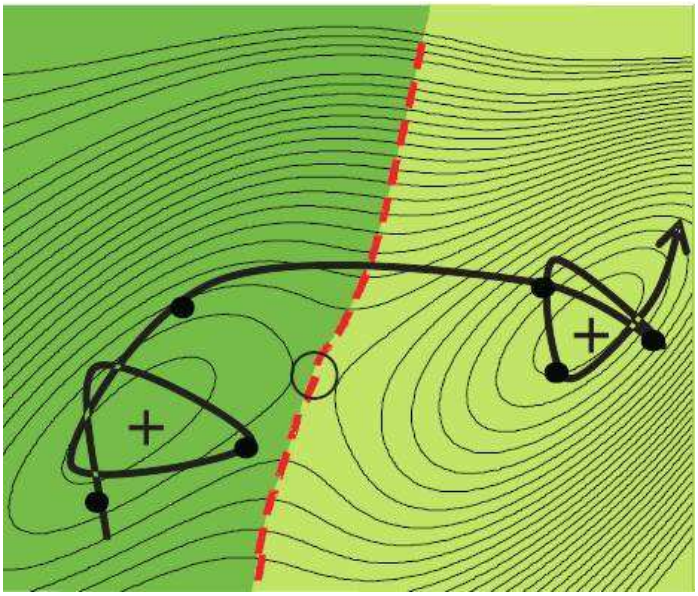

Figure 1.6: Sketch of a 2D landscape together with the inherent states (crosses), transition state (open circle) and basin border (dashed line). The solid line indicates a possible molecular dynamics trajectory at low temperatures. The solid circles denote the positions of the system from which the minimization procedure may have started, respectively. For that case both minima would be found exactly three times as the result of a minimization via steepest descent. Reprinted by permission from IOP Publishing [21]. Link: doi:10.1088/0953-8984/19/20/205143

of as the exploration of various topographical configurations on the potential energy surface, with transitions between adjacent inherent structures.

Although potential energy landscape provides a practical perspective for glass transition, it is not a complete description of glass transition at finite temperature. Free energy landscapes have energetic and entropic component, $F = U - TS$. At low temperature when $T \to 0$, the contribution of entropy is neglectable, so the potential energy landscape is T-independent. Wallace's work highlights the importance of configurational entropy in finite temperature system using vibrational-traditional theory [23]. By incorporating other thermodynamic variables, such as configurational entropy, the free energy landscape provides a more complete understanding of the glass transition. The free energy landscape is the free energy as a function of the system configuration which has many local minima [24]. Computational research on the free energy landscape of colloidal glasses indicates that the system can take a variety of routes to reach a metastable state due the complexity of free energy landscape.

The cooperative rearrangement proposed by Adam and Gibbs is a functional concept for understanding the transition between inherent structures in free energy landscape [25]. In cooperative rearrangement events, the transition between local minima involves more particles/atoms in a 'simultaneously rearranged region'. In Chap. 2.3, we study the cooperative rearrangements between local minima in a glassy system.

For many-body systems, the potential energy landscape or free energy landscape can be extraordinarily complex. In a system with N particles, the complete energy landscape is a surface in $(3N + 1)$-dimensional space, which is impossible to be demonstrated as is in graph Fig. 1.5. So one important problem in using the energy

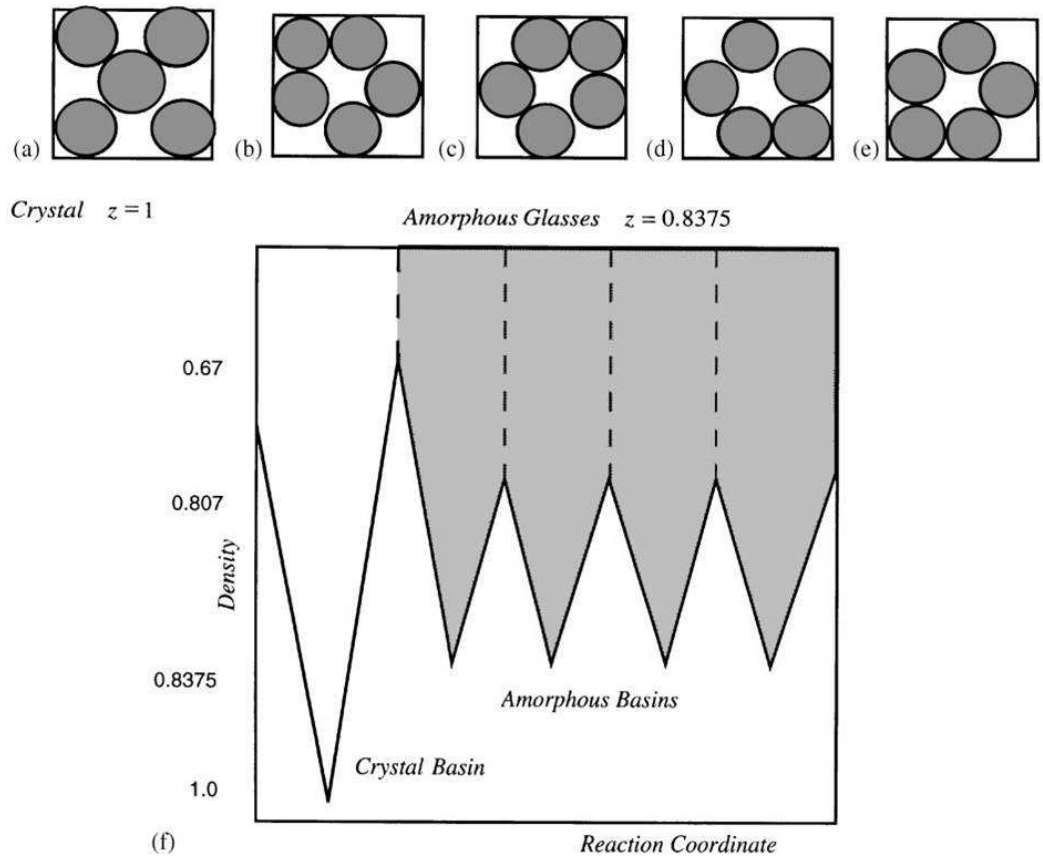

Figure 1.7: The inherent structures and density configuration surface for five discs in a box. The most dense packing (a) is the crystal and structures (b e) are the glasses. (f) is the density configuration surface. Density increases down the vertical axis and the horizontal axis represents the $2N$-dimensional reaction coordinate. Reprint with permission from [26]. License Number; 3961410910803.

landscape approach to understand glass transition is reducing the number of spatial coordinates while still adequately presenting the features of the system [17, 27, 28]. Low-dimensional projection is applied to some research work, which is studying how the energy of a system evolves in a one or two-dimensional space with one or two atom coordinates of interest [29–31]. Furthermore, to reduce the complexity glassy system and fully understand the energy landscape in glass transition, researchers build up simple models and study the transitions between inherent structures in energy landscape. In a simple model, there are only a few inherent structures (or local minima), so the landscape can be fully characterized in terms of local minima and the energy barriers. Figure 1.7 is one example of simple model [26]. It consists of five hard equal-sized disks confined in a square confinement. Figure 1.7(a-e) shows the five inherent structures. Figure 1.7(a) is the most probable structure which could be considered as a crystal state, while the four orientationally distinct lower density inherent structures are called the glasses or amorphous structures of the model. Figure 1.7(f) is a very schematic representation of the density configuration surface in which the five inherent structures correspond to the bottom of the basins. The transitions between the inherent structures involves cooperative rearrangements of the five particles. The simplicity of the density configuration surface of five discs in a box makes possible the detailed analysis of the transitions between metastable states of the fluid in terms of the inherent structures. In the spirit of this model, in Chap. 2, we introduce a very simple model with three disks confined in a circular confinement, in which there are two energy local minima(or inherent structures) and one transition state. By simulating the Brownian motion of the disks and calculating the probability

of each configuration in the system, we are able to accurately present the free energy landscape in one-dimensional space with one reaction coordinate. Since soft particles interacting with potential energy in glassy systems, they could be considered as a hard particle with a smaller effective size. In Chap. 3.1, we introduce a way to map particles with soft interaction potentials onto hard particles with some effective size by treating the particles in a pair-wise fashion. And this method works our simulation models with finite-range potentials. To develop the simulation method for glassy system, we introduce forward flux sampling as a convenient and efficient method to calculate long time scale for the local rearrangement in Chap. 2. It successfully provides the information of the dynamics in glassy systems which is infeasible using the traditional brute-force method. The computational results are consistent with our theoretical conjectures in Chap. 2.3.3.

Chapter 2

Energy barriers, entropy barriers, and non-Arrhenius behavior in a minimal glassy model

2.1 Introduction

Glassy materials are amorphous solids: disordered microscopically, and unable to flow macroscopically [32–35]. They are inherently out of equilibrium [36, 37], in contrast to crystals. In 1969, Goldstein proposed the idea of the potential energy landscape, a conceptual framework for thinking about glassy and crystalline materials [19]. The potential energy landscape is defined as the potential energy U of a material "plotted as a function of $3N$ atomic coordinates in a $3N + 1$ dimensional space," where N is the number of atoms [19]. At low temperatures, an ideal crystalline solid will have particle coordinates that correspond to a global minimum of the potential

energy landscape. Glasses are disordered, so at low temperatures a glass will have coordinates in a local minimum of the potential energy landscape, but there are an enormous number of such local minima [21, 38–40].

Turning to higher temperatures where a material is a liquid, thermal energy allows the system to rearrange constantly, and so the $3N$ atomic coordinates trace out a trajectory traversing the potential energy landscape. If the temperature is close to the material's glass transition, and if crystallization is avoided, then the trajectory through the landscape spends most of its time near local minima, with occasional passages through a saddle point in the landscape to an adjacent minimum [41, 42]. The number of minima, their depth, and the details of the saddles between them can be connected to the microscopic dynamics of samples at a variety of temperatures [21, 40]. At low temperatures, the thermal energy k_BT does not allow the system to escape a local minimum easily. In particular the escape from any particular local minimum is a thermally activated process, depending on the barrier height between that local minimum and the minima adjacent in the $3N + 1$ dimensional space. Of course, given the high dimensionality of the problem, visualizing this is impossible except for conceptual sketches [39, 43, 44], of which the earliest one we are aware of was by Stillinger and Weber in 1984 [45].

The picture of a potential energy landscape changes when one considers a system of hard spheres. Hard spheres are defined as particles that have no interaction energy when they are not in contact, and infinite interaction energy if they touch. As a function of the $3N$ sphere coordinates, the potential energy surface is flat at $U = 0$ except for prohibited configurations for which $U = \infty$. Rather than local minima

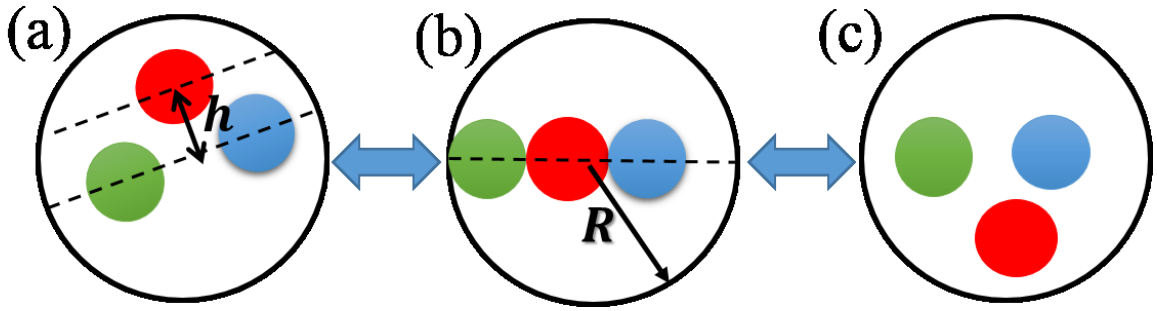

Figure 2.1: (Color online) Sketch of our model, with three distinguishable particles confined within a circular system. In (a), h is the distance between one of the particles and the axis defined by the other two. In (b), R is the radius of the confining boundary. The states (a)-(c) show a cage breaking event in our model, where h changes sign.

separated by saddles, the landscape has flat open areas separated by bottlenecks that correspond to *entropic* barriers. As hard spheres can form glasses at high densities [46–48], these entropic barriers must function similarly to the potential energy barriers in a potential energy landscape [49–51].

In 2012 Hunter and Weeks introduced a simple model with hard particles where the entropic landscape was directly measurable [51]. The model consists of three hard disks executing Brownian motion within a two-dimensional circular region. As illustrated in Fig. 2.1, the system has two distinct configurations of the three disks. A transition occurs between these two configurations when any one of the three particles passes between the other two. When the system size R is smaller, these transitions are rarer. This model captures the flavor of hard spheres near their glass transition, where rearrangements are difficult due to particle crowding [52, 53]. Hunter and Weeks directly calculated a free energy landscape based entirely on the entropy of the states. They demonstrated that the transition time scale was related to the

entropic barrier height, $\tau \sim \exp(S_b)$.

In the current manuscript, we extend the model of Hunter and Weeks to consider the case of soft particles. In this situation, we now have a potential energy landscape that varies smoothly as a function of the particle coordinates. However, the best description of our model is through the free energy landscape which includes both entropy and potential energy. The transition state shown in Fig. 2.1(b) still corresponds to a barrier, now with both potential energy and entropic components. For finite-range interaction potentials, we use simulations to see how the free energy landscape approaches the hard disk case as $T \to 0$. For all potentials, we examine potential energy and entropy to understand the relative importance of each in determining the transition rate between states. Our most significant result is an explicit demonstration that the influences of both potential energy and entropy depend on temperature; that is, the effective free energy barrier height depends on T. Our results help bridge concepts between soft and hard particles in a simple model, complementing prior molecular dynamics simulations done with large numbers of soft particles [9, 54, 55].

Our model is a straightforward system with non-Arrhenius scaling as the glass transition is approached. Arrhenius scaling occurs in a system where a time scale τ for a transition is set by a fixed energy barrier of size Δ, such that $\tau \sim \exp(-\Delta/k_B T)$. In a glass-forming system, τ could be the time scale for diffusion or flow, and τ grows dramatically as the glass transition is approached. Often, this happens in a non-Arrhenius fashion [56]: τ grows faster than expected as T is decreased. This leads to the interpretation that $\Delta = \Delta(T)$ increases as T decreases. We demonstrate that in our model Δ is due to potential energy and entropy, both of which are T-dependent,

even though the underlying potential energy landscape is T-independent.

2.2 The Model System

We study three two-dimensional particles confined to a circular system of size R as shown in Fig. 2.1. We will consider four distinct particle interactions in our simple model system.

Our first particle type is a commonly used finite-ranged harmonic potential [57, 58]. This considers deformable soft particles interacting through purely repulsive body centered forces. Our harmonic potential is defined as:

$$U_{\mathrm{HM}}(r_{ij}) = \begin{cases} U_0(\frac{2-r_{ij}}{2})^2; & r_{ij} < 2 \\ 0; & r_{ij} \geq 2 \end{cases} \tag{2.1}$$

Here r_{ij} is the center-to-center distance between particles i and j. All particles have radius 1 ($a_i = a_j = 1$) and do not interact when they are not touching ($r_{ij} \geq 2$). The particles have the same interaction with the wall:

$$U_{\mathrm{HM,wall}}(r_{ic}) = \begin{cases} U_0(\frac{r_{ic}-(R-1)}{2})^2; & r_{ic} > R-1 \\ 0; & r_{ic} \leq R-1 \end{cases} \tag{2.2}$$

r_{ic} is the distance between the particle center and system center, that is, it is the radial coordinate of particle i. As the particle radius is 1, when $r_{ic} = R-1$ the particle comes into contact with the wall, and for $r_{ic} > R-1$, the interaction energy increases and the particle feels a repulsive force from the wall.

Our second particle type is also repulsive, but has a infinite range interaction between the particles, and between the particles and the wall; we term this the "long-

range potential." We define this potential as:

$$U_{\mathrm{LR}}(r_{ij}) = U_0(\frac{r_{ij}}{2})^{-12} \tag{2.3}$$

between the particles and

$$U_{\mathrm{LR,wall}}(r_{ic}) = U_0(\frac{R - r_{ic}}{2})^{-12} \tag{2.4}$$

between the particles and the wall.

Our third particle type uses the Lennard-Jones potential ("LJ potential"), which approximates the interaction between a pair of neutral atoms [59]. The Lennard-Jones potential is defined as:

$$U_{\mathrm{LJ}}(r_{ij}) = U_0(\frac{r_{ij}}{2})^{-12} - U_0(\frac{r_{ij}}{2})^{-6}. \tag{2.5}$$

This interaction potential differs from the first two (harmonic and long-range) in that Lennard-Jones particles have both a repulsive and an attractive component. In contrast to the first two potentials, these particles have a finite preferred separation distance that minimizes U at $r_{ij} = 2^{7/6} = 2.245$. To simplify this model, the wall is hard. In this case, the interaction energy with the wall is $U = 0$ until the particles touch the wall ($r_{ic} = R - 1$) in which case $U = \infty$.

We consider one last particle type using the Weeks-Chandler-Andersen potential ("WCA potential") [60]. This potential starts with the LJ potential, truncates it at the minimum, and then shifts it upward so that the potential goes smoothly to zero:

$$U_{\mathrm{WCA}}(r_{ij}) = \begin{cases} U_{LJ} + \frac{U_0}{4}; & r_{ij} < 2^{7/6} \\ 0; & r_{ij} \geq 2^{7/6} \end{cases} \tag{2.6}$$

This then is the repulsive component of the LJ potential, and has no attractive component. As with the LJ potential, we again assume a strictly hard contact with

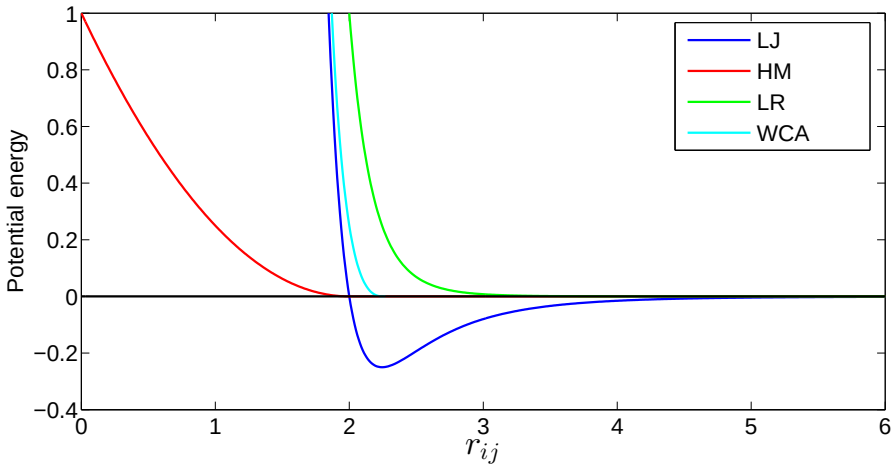

Figure 2.2: (Color online) Various potential energy as a function of the center-to-center distance between two particles, r_{ij}. Red curve is harmonic potential energy (HM). Dark blue curve is Lennard-Jones potential energy (LJ). Light blue curve is Weeks-Chandler-Andersen potential energy (WCA). Green curve is long-range potential energy (LR).

the confining wall. Like the harmonic potential, the WCA potential is finite-ranged, but in contrast this potential diverges at $r_{ij} \to 0$. This latter behavior is like the long-range potential, which also diverges.

As is shown in Fig. 2.2, these four interaction potentials capture several interesting possibilities. Two are finite-ranged; three are purely repulsive; three diverge as the particle separation goes to zero.

We use the Metropolis algorithm [61] to simulate Brownian motion of the particles, similar to previous work by our group [51]. At each Monte Carlo step, we try to move each particle (one at a time) in a random direction with *rms* step size of 0.01 (or in some cases smaller). We consider the change in energy ΔU for the trial move. These trial moves are accepted with probability 1 if $\Delta U < 0$, and with probability $\exp(-\beta\Delta U)$ otherwise, with $\beta = 1/k_B T$. The initial condition is with the three

particles starting at the vertices of an equilateral triangle of side length 2, and the system is equilibrated after the first transition of the sort shown in Fig. 2.1. The simulation was evolved continuously for at least 20 transitions, (in the cases with very slow dynamics) and more typically 100-1000 transitions. Given that there is no memory in this system, each condition was run only once as a time-average was adequate (although we did check this with multiple runs several times, and also checked that the results are insensitive to the *rms* step size).

In all situations, the radius of the confined system is R as indicated in Fig. 2.1. For the harmonic potential, recall the particle radius is 1, so for $R = 3$ the particles can just line up across a diameter of the system with $U = 0$. For $R < 3$, particles can only change configuration [Fig. 2.1(a-c)] with a nonzero temperature. The WCA potential is also finite-ranged, although the range is not 1 but rather $2^{7/6}$, so here $R = 1 + 2^{\frac{7}{6}} = 3.245$ is the smallest radius at which particles can line up across a diameter with $U = 0$. For the long-range potential and the LJ potential, particles always interact with nonzero potential energy, and so there is no value of R with any special meaning.

Note that the meaning of U_0 differs between the potentials in an unimportant way. For the harmonic potential, U_0 is the maximum potential energy between two particles when they are fully overlapped ($r_{ij} = 0$). For the long-range potential, U_0 is the potential energy between two particles when $r_{ij} = 2$. For LJ and WCA, there are yet other meanings for U_0. In the simulation, we simply set $U_0 = 1$ and vary the value of k_BT. As U_0 is not comparable between the different interactions, likewise specific values of T are not comparable either. Accordingly, our discussion will focus

on comparing behaviors as functions of T without need to compare specific values. The remainder of the paper will study the behavior of our model as we change R, T, and the interaction potential. In particular we are most interested as the system becomes "glassy:" smaller R and/or smaller T.

2.3 Results

2.3.1 Free energy landscapes

To study the free energy landscape, we define a macrostate variable h as is shown in Fig. 2.1(a) [51]. To do this, we pick two particles to define an axis (say, pointing from particle 1 to particle 2). h is the distance of the third particle above (or below) this axis. h can be positive or negative, and is zero at the transition state shown in Fig. 2.1(b). Therefore, when h changes sign, a rearrangement occurs. It is arbitrary which particles are used to define the horizontal axis; if we consider h' and h'' defined using different pairs of particles, all three h variables change sign simultaneously upon a transition [51].

Following Ref. [51], we construct the free energy landscape by counting occurrences of each h in the simulation for given parameters (R and T). We then compute $P(h)$, the probability of seeing each h value. Finally, the free energy landscape is computed directly according to the Boltzmann distribution, $P(h) \sim \exp(-F(h)/k_B T)$. For simplicity, we set $k_B = 1$ in the simulation. We shift $F(h)$ so that the minimum value is $F = 0$.

Figure 2.3(a) shows the free energy landscape for the harmonic potential model.

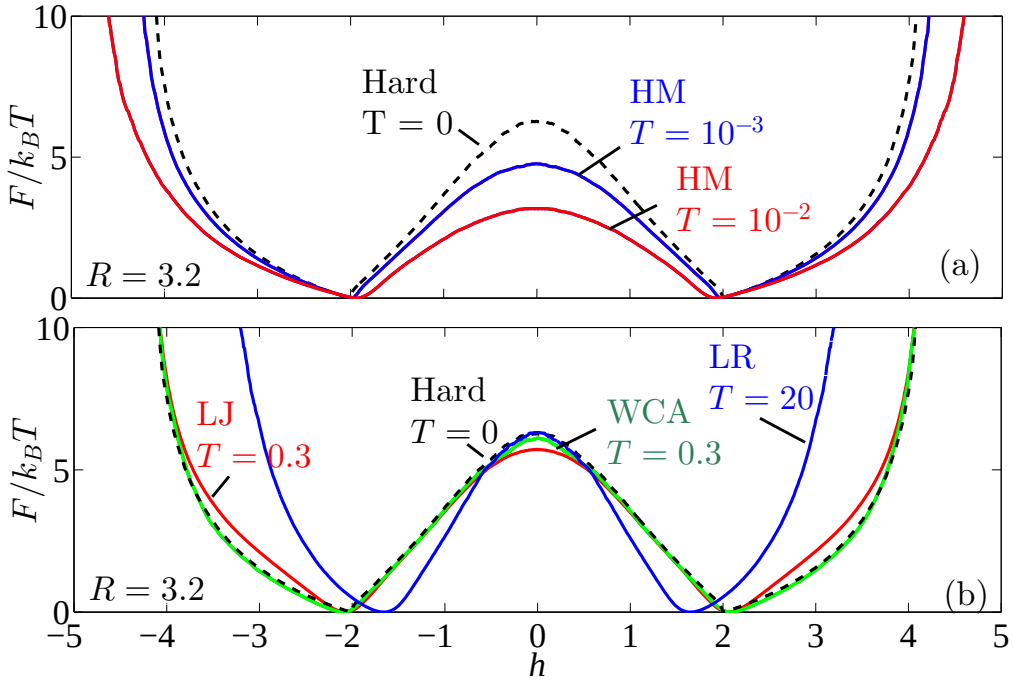

Figure 2.3: (Color online) (a) The free energy landscape for the harmonic ("HM") interaction potential. $R = 3.2$ and the temperatures are as indicated. (b) Free energy landscapes for interactions as indicated, where "LR" designates the long-range potential, "LJ" the Lennard-Jones potential, and "WCA" the Weeks-Chandler-Andersen potential. $R = 3.2$ and the temperatures are as indicated, chosen so that the barrier height at $h = 0$ is comparable for the different interaction potentials.

There is a free energy barrier at the transition state $h = 0$. For $R = 3.2$, the particles do not have to overlap at the transition state, but for $T > 0$ they are allowed to overlap which makes transitions easier. Keeping R fixed, as $T \to 0$ overlaps are less likely, and the free energy barrier for transitions grows. At $T = 0$, overlaps are impossible, although since this is a finite-range potential, transitions still occur. In this situation the free energy landscape is identical to the landscape for hard disks, indicated by the dashed line in Fig. 2.3(a). In other words, at low T, thermal fluctuations decrease and these soft particles become hard.

The other features of the free energy landscape shown in Fig. 2.3(a) are straightforward to understand. There are two symmetrically located minima close to $h = \pm 2$ that correspond to the most probable states for the three particles [51]. For large values of $|h|$, the particles are forced to interact with the confining wall. This causes the free energy to grow dramatically due to the large potential energy penalty.

Figure 2.3(b) shows free energy landscapes for other interaction potentials, with temperatures chosen so that the barrier height is approximately the same for each, and $R = 3.2$ kept constant. The shapes are all qualitatively similar, although the long range potential has particles confined to a smaller range of h. For the hard particle case, the minima occur precisely at $h = \pm 2$ [51]. For the other potentials, the locations of the minima vary with T. For the LR and LJ potentials, one can compute the configuration that minimizes U, and the h that minimize $F(h)$ are fairly close to the h for those minimal U configurations. The T dependence, however, makes it clear that minimizing the free energy is not the same as minimizing the potential energy. Maximizing entropy plays a role as well in determining the h that minimizes $F(h)$. As previously reported, in the hard model, $\partial F/\partial h$ is discontinuous at $h = \pm 2$ [51]. However, this derivative is continuous everywhere in all of the soft models.

2.3.2 Dynamics and free energy barriers

The dynamics are straightforward when considering $h(t)$. Often, $h(t)$ stays close to the values $h_{\min}$ that minimize the free energy landscape (Fig. 2.3), but occasionally $h(t)$ switches sign. We quantify the dynamics by plotting the mean square displacement (MSD) $\langle \Delta h^2 \rangle$ as a function of lag time Δt in Fig. 2.4 for the harmonic potential

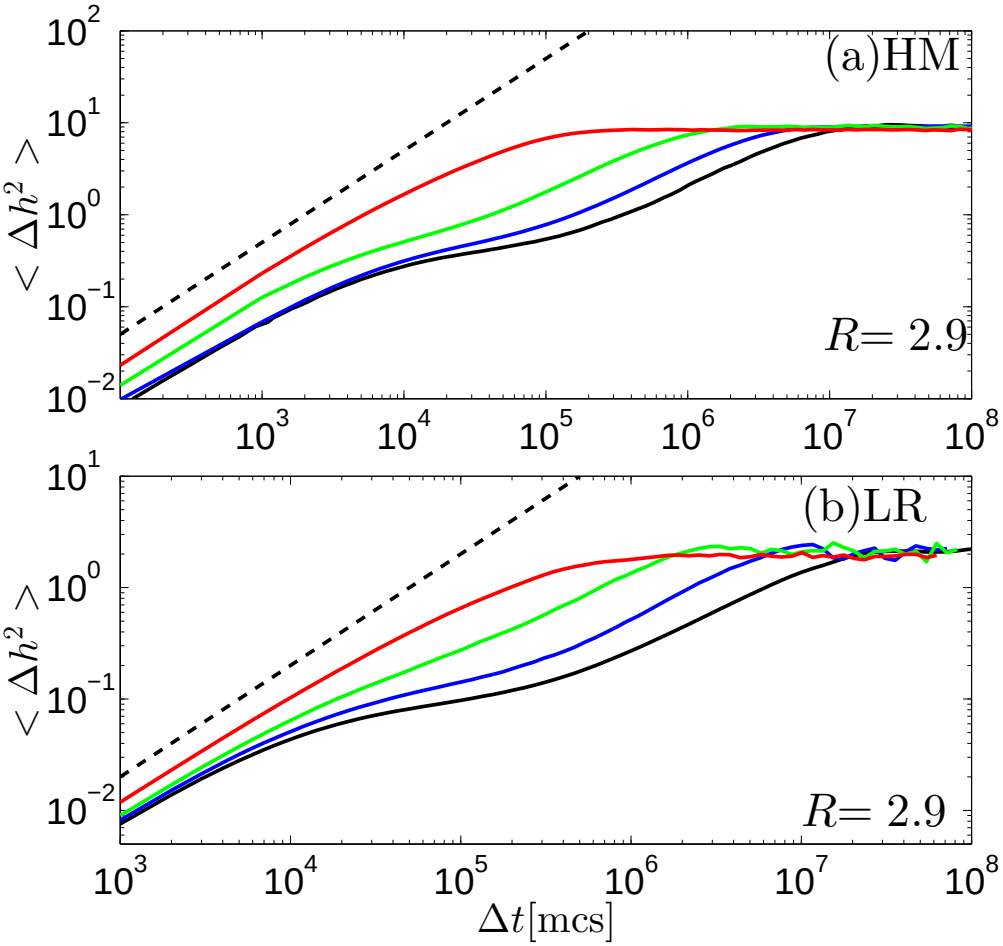

Figure 2.4: (Color online) (a) Mean-square displacement in h space for the harmonic ("HM") interaction potential. $R = 2.9$ and $T = 10^{-1}, 10^{-2}, 10^{-2.2}, 10^{-2.4}$ (from top to bottom, red to black). The dashed line has a slope of 1. (b) Mean-square displacement in h space for the long-range ("LR") interaction potential. $R = 2.9$ and $T = 10^{6}, 10^{4.6}, 10^{4.2}, 10^{4}$ (from top to bottom, red to black). The dashed line has a slope of 1.

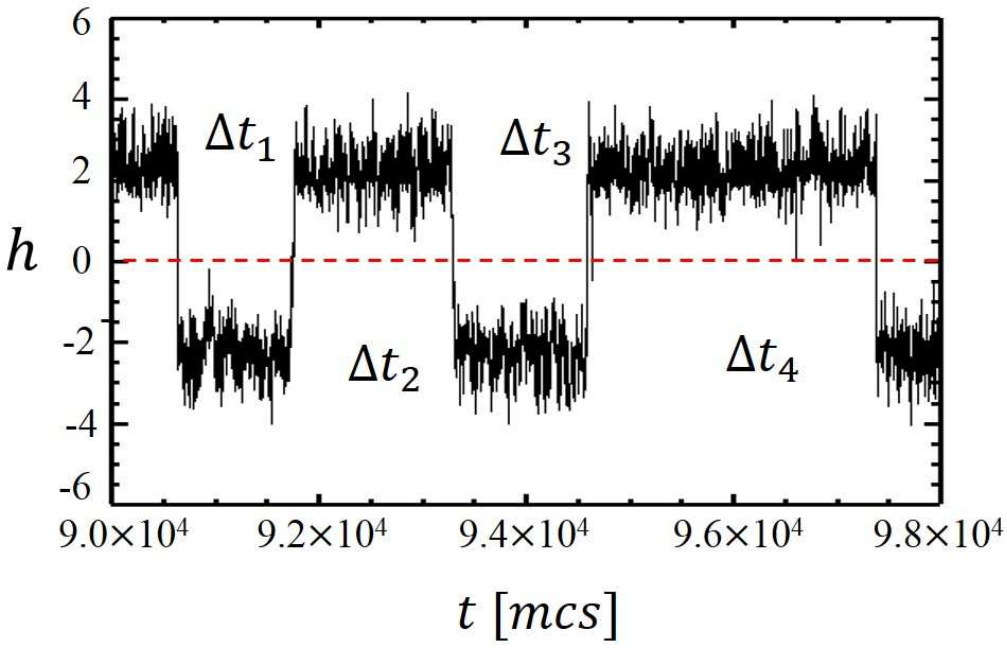

Figure 2.5: (Color online) A trajectory through h space. Red dashed line passes through $h = 0$. Small fluctuations about $h = 0$ are not considered as true transition events. Five transition events occur during this trajectory. The length of time between crossing events are denoted as Δt_1, Δt_2, Δt_3 and Δt_4. The transition time scale is defined as the average of the time intervals, $\tau =< \Delta t_i >$, during the trajectory.

(a) and long-range potential (b). At the shortest times, particles diffuse fairly freely. At intermediate time scales, the MSD starts to level off, reflecting that the system is trapped in one of the probable states shown in Fig. 2.1(a,c). At longer time scales, the system can swap between these two states, and the MSD begins to rise again. At the longest time scales shown in Fig. 2.4, the MSD levels off due to the finite system size.

To quantify the transition time scale τ, we measure the average time between sign changes of h, as is shown in Fig. 2.5. However, during a transition, there are often small fluctuations right around $h = 0$ that are not true transitions. To avoid biasing

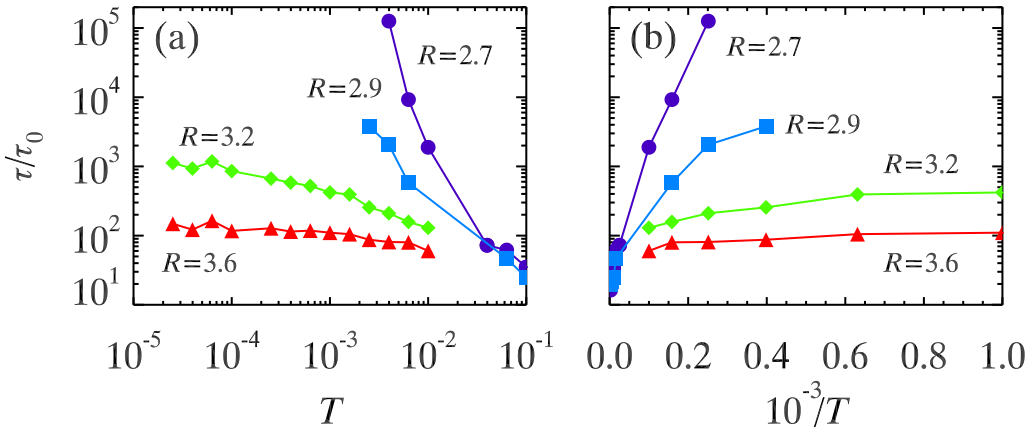

Figure 2.6: (Color online) Dependence of τ on T and R in harmonic potential system. Curves in different colors show the life time as a function of T with different R as indicated. The lifetimes τ are normalized by $\tau_0 = 1/2D$, the time a free particle would take on average to diffuse a distance of 1, using the diffusion constant D from the simulation.

τ toward lower time scales, we stipulate that once $h = 0$ is crossed, the system must move a further distance $\Delta h = 1$ before returning [51]; our results are not sensitive to this choice. The probability distribution of time scales $P(\tau)$ is exponentially distributed so the mean value gives the appropriate time scale, which we plot in Fig. 2.6 as a function of temperature (a) and inverse temperature (b). The two largest system sizes R show a horizontal leveling off of τ at cold temperatures. This is the limit where the soft particles behave as hard particles, and τ reaches the value seen for purely hard particles [51]. For the smaller system sizes, particles must overlap to have a transition, and so as $T \to 0$ this becomes rare and τ diverges. Were any of these systems to be Arrhenius with a temperature-independent potential energy barrier, the data in Fig. 2.6(b) would fall on a straight line; that they do not indicates that the system is non-Arrhenius.

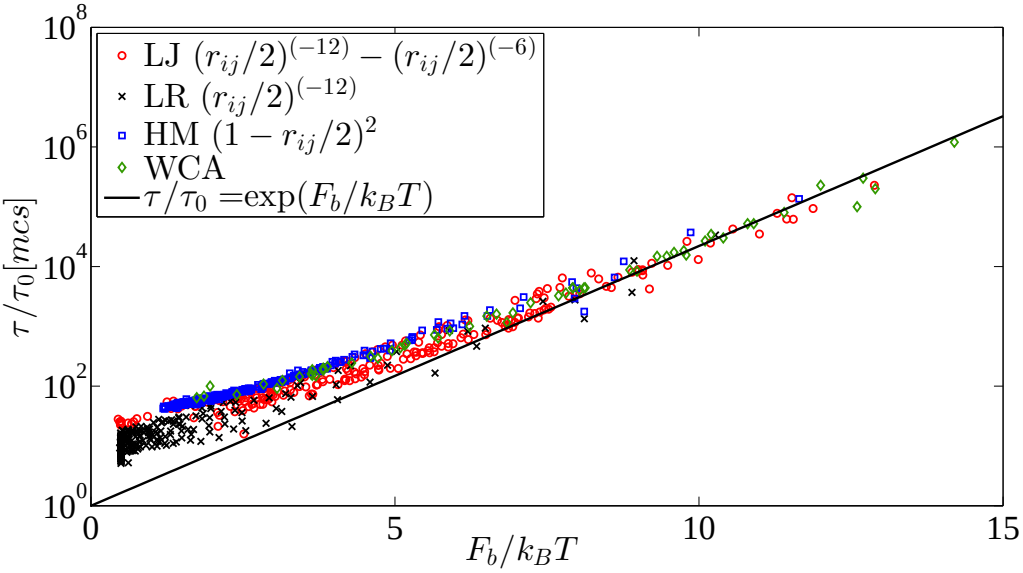

Figure 2.7: The lifetime grows exponentially with the free energy barrier F_b as $F_b \to \infty$, as indicated by the solid line. The symbols are as indicated, and correspond to a variety of R and T values; for specific ranges of R and T, see ranges shown in Figs. 2.6, 2.8, and 2.11.

An alternate way to think of Arrhenius behavior is in terms of the free energy barrier for transitions, F_b. Calculating the free energy landscapes as in Fig. 2.3 allows us to determine $F_b = F(h = 0)$. Transitions are less frequent with higher F_b. Figure 2.7 verifies that τ grows Arrheniusly as a function of F_b, $\tau \sim \exp(\beta F_b)$ as $F_b \to \infty$. The deviations seen for small F_b are due to large system sizes: for larger systems, it simply takes longer for particles to move to the transition state [51]. The details of this vary depending on the potential. Additionally, the vertical spread of symbols for a given potential for $F_b \lesssim 5$ reflects that different R and T values can have the same F_b. Nonetheless, the collapse of the data at larger F_b indicates that τ grows Arrheniusly with F_b precisely where the dynamics are slowest.

Our primary interest is understanding the cause of glassy dynamics in our system. In other words, we'd like to understand how τ grows large (equivalently, how F_b grows large) as we decrease T and/or decrease R. Figure 2.8 shows F_b/k_BT as a function of T for different particle types. In each panel, the different curves are for different system sizes R. As expected, F_b/k_BT grows with decreasing T and with decreasing R. Panels (a) and (b) show some curves with qualitatively different behavior, in that F_b/k_BT goes to a plateau as $T \to 0$. As with Fig. 2.6, this is because of the behavior of the free energy landscape shown in Fig. 2.3(a) for these two finite-ranged potentials: for large system sizes R, even at $T = 0$ the particles can rearrange without overlapping. For large R, the plateau values for F_b seen in Fig. 2.8(a,b) are precisely the free energy barrier heights for hard disks [51]. For this argument to work, the system size R must exceed a critical value, $R_c = 3$ for the harmonic potential and $R_c = 3.245$ for the WCA potential (as discussed at the end of Sec. 2.2). For $R < R_c$,

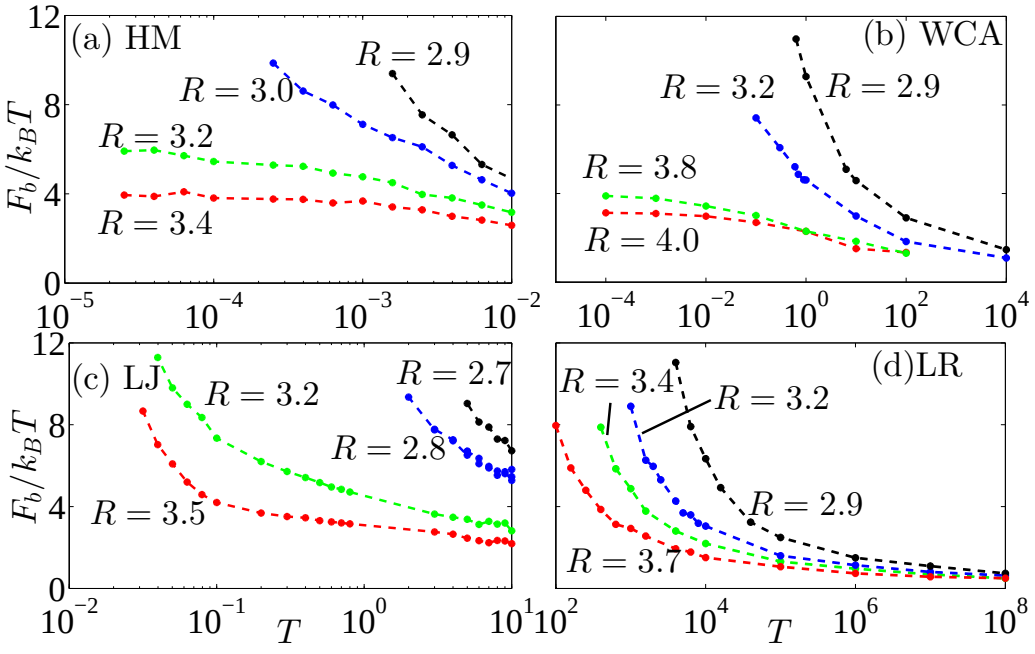

Figure 2.8: (Color online) Dependence of $\frac{F_b}{k_BT}$ on T and R. Curves in different colors show the free energy barrier as a function of T with different R as indicated. The interaction potentials are (a) harmonic ("HM"), (b) WCA, (c) Lennard-Jones, (d) long-range ("LR"). (As discussed in Sec. 2.2, recall that the specific values of T are not comparable between the different potentials.)

particles must overlap at $h = 0$ with $U > 0$, and so as $T \to 0$ the free energy barrier F_b will diverge. For the LJ and LR potentials, at $h = 0$ we always have $U > 0$ and so not surprisingly F_b diverges in all cases at low temperatures, with the details depending on R.

These behaviors raise an interesting question. In the cases of Fig. 2.8(a,b) with a plateau, the system approaches the hard disk behavior as $T \to 0$. For hard disks, this free energy barrier is entirely an entropic barrier [51]. However, clearly for many other cases in Fig. 2.8, the free energy barrier is at least in part due to the potential energy component of the barrier. To what extent in any of these cases can the free energy barrier be ascribed to entropy, and to what extent to potential energy?

2.3.3 Simple models for the transition state

To understand the interplay of entropy and potential energy at the transition state ($h = 0$) for our three particle system, we consider a simple model for the transition state. Consider a system moving along a reaction coordinate h with a flat energy landscape, except for a barrier at $h = 0$. At $h = 0$, we will assume there is a second coordinate x in the orthogonal direction. In the three particle system, this would account for other degrees of freedom for the particle locations subject to the constraint $h = 0$. We examine three ideas for $U(x)$, sketched in Fig. 2.9.

First consider Model 1 [Fig. 2.9(a)], where we let x be constrained on the interval $0 \leq x \leq 1$ and the potential energy barrier depends on x as:

$$U(x) = 0, \quad 0 \leq x < \delta \tag{2.7}$$

$$U(x) = U_0, \quad \delta \leq x \leq 1 \tag{2.8}$$

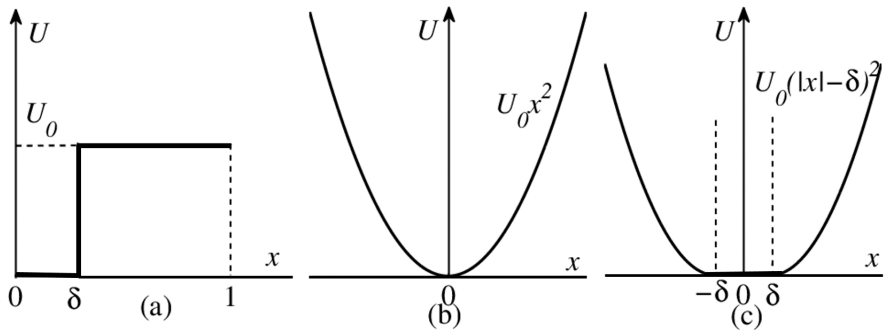

Figure 2.9: Sketch of three simple potential energy landscapes. (a) Model 1. (b) Model 2. (c) Model 3.

so that the system can either make a transition at zero potential energy cost, or with a finite cost $U_0 > 0$.

Attempts to cross with zero potential energy cost occur with probability

$$p_1 = \delta \tag{2.9}$$

and these attempts always succeed. Attempts to cross elsewhere occur with probability $(1 - \delta)$ and succeed with probability $\exp(-U_0/k_BT)$; thus the likelihood of a barrier crossing taking this pathway is

$$p_2 = (1 - \delta) \exp(-U_0/k_BT). \tag{2.10}$$

The crossing attempt entirely fails with probability $1 - p_1 - p_2$. If attempts are made with a time scale τ_0, then the mean transition time can be shown to be

$$\tau = \frac{\tau_0}{p_1 + p_2}. \tag{2.11}$$

The question to consider, then, is what this transition looks like in terms of a free energy barrier, if we average over the coordinate x? Two limits are immediately

obvious. If U_0/k_BT is sufficiently large, $p_1 \gg p_2$ and the transition rate is governed by an entropic barrier. In the converse limit, if δ is sufficiently small, the $U = 0$ pathway is vanishingly rare ($p_1 \ll p_2$) and transitions are governed by the potential energy barrier U_0. In between these limits, one can think of this system as having an effective free energy barrier that is due to both potential energy and entropy. The mean potential energy the system has when the barrier is crossed is given by

$$\beta\langle U\rangle = \frac{\beta U_0 p_2}{p_1 + p_2} \tag{2.12}$$

using $\beta = 1/k_BT$. The partition function at the crossing is given by $Z = p_1 + p_2$, the free energy barrier height is $\beta F = -\ln Z = -\ln(p_1 + p_2)$, and the entropy can be derived as

$$\beta TS = -\beta T\frac{\partial F}{\partial T} = \ln(p_1 + p_2) + \beta\langle U\rangle \tag{2.13}$$

(which is also apparent from $F = U - TS$).

The conclusion is that while the potential energy surface is T-independent and always has a $U = 0$ transition pathway, the free energy barrier depends on T and on average requires nonzero potential energy for the transition. Given that p_2 depends on T, Eqns. 2.12 and 2.13 show that both the potential energy and entropy contributions to the free energy barrier depend on T.

We next consider the more realistic Model 2, where the transition has a harmonic potential with respect to the coordinate x:

$$U(x) = U_0 x^2. \tag{2.14}$$

For this potential, the mean potential energy required is $\beta\langle U\rangle = 1/2$ (equipartition). In the interesting limit $T \to 0$, the free energy barrier grows as $\beta F \sim |\ln T|$. As the potential energy contribution is independent of T, the barrier growth is due to entropy: at low temperatures the system only crosses at $|x| \lesssim \sqrt{k_B T/U_0}$. As with Model 1, while $U(x)$ is independent of T, the free energy barrier depends on T.

Finally, we consider model 3 which is a hybrid of the previous two models:

$$U(x) = 0, \quad |x| < \delta \tag{2.15}$$

$$U(x) = U_0(|x| - \delta)^2, \quad |x| \geq \delta. \tag{2.16}$$

In this model, the mean potential energy required to cross the barrier is $\beta\langle U\rangle = \frac{1}{2}(1 + 2\delta\sqrt{\frac{\beta U_0}{\pi}})^{-1}$. At low temperature and with large δ, the system prefers to cross within the region $|x| < \delta$ where potential energy is zero. In this case, $\delta\sqrt{\frac{\beta U_0}{\pi}} \to \infty$, and $\beta\langle U\rangle \to 0$. For small δ and/or large T, the average potential energy found when crossing the barrier is larger. At high temperature and with small δ, when $\delta\sqrt{\frac{\beta U_0}{\pi}} \to 0$, $\beta\langle U\rangle \to 1/2$, which is same as model 2.

To be clear, for these models we are really interested in the case where the system climbs a potential energy hill to reach the transition state $h = 0$. We are then considering how the system crosses through the $h = 0$ state, and concluding that this requires additional potential energy (on average) and also navigating an entropic barrier. In other words, merely having enough potential energy to reach the saddle is insufficient, as threading through the saddle's lowest point is of low probability. In all of these simple models of the transition state, the transition time scale will be

$$\tau = \tau_0 \exp(\beta U_{\min}) \exp(\beta F) \tag{2.17}$$

where $U_{\min}$ is the potential energy of the saddle's lowest point, and F is the additional free energy barrier associated with the $h = 0$ potential energy landscape cross-section. The $\exp(\beta U_{\min})$ contribution gives Arrhenius scaling with T, and the $\exp(\beta F)$ contribution provides additional non-Arrhenius scaling as F grows with decreasing T, as shown above. In many situations, the $\exp(\beta U_{\min})$ term dominates, but it depends on the details as will be shown below.

2.3.4 Barriers: Energy and Entropy

This discussion motivates us to divide the free energy barrier in our three-particle simulations into energetic and entropic components. As $F = U - TS$, we consider the free energy barrier to be:

$$\beta F_b = \beta U_b + S_b \tag{2.18}$$

where as usual, $k_B = 1$. The relevant quantities are illustrated in Fig. 2.10. $h_{\min}$ is the value of h that minimizes the free energy. The contribution of potential energy to the barrier is defined as $U_b = \langle U \rangle(0) - \langle U \rangle(h_{\min})$. $\langle U \rangle$ is the black curve indicated by U_b in Fig. 2.10, and is averaged over ≥ 20 barrier crossings. Equation 2.18 lets us calculate S_b from F_b and U_b. Note that the definition of S_b differs from U_b by a minus sign: $S_b = S(h_{\min}) - S(h) > 0$, such that it is positive (and thus a barrier). The minimum possible potential energy for each value of h is the thin red curve in Fig. 2.10 which is at zero for most values of h. We define $U_{\min}$ as the minimum potential energy needed to cross $h = 0$ if the system finds the optimum transition path, as indicated in Fig. 2.10. It is clear from Fig. 2.10 that U_b will almost always be larger than $U_{\min}$, although a rare exception for the Lennard-Jones potential will be described below.

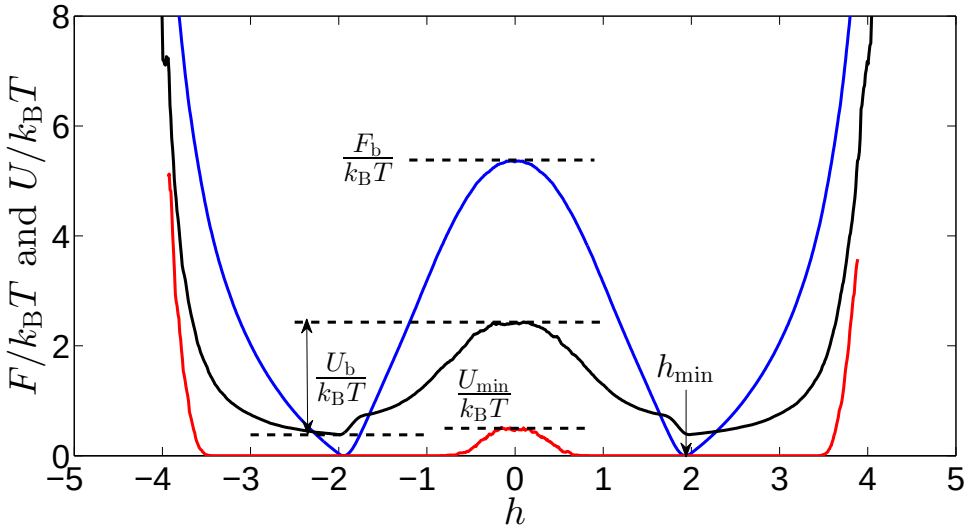

Figure 2.10: (Color online) The free energy landscape for the harmonic ("HM") interaction potential. $R = 2.9$ and $T = 10^{-2.2}$.The blue curve is the free energy landscape. The black curve is the potential energy landscape based on $\langle U \rangle$ in h space. The red curve is the minimum potential energy, $U_{\rm min}$, in h space. F_b/k_BT, U_b/k_BT, and $U_{\rm min}/k_BT$ are as indicated. $h_{\rm min}$ is the value that minimizes F.

$U_{\rm min}$ is a quantity we can derive analytically for each interaction potential, while U_b is determined from the simulation data. $U_{\rm min}$ is temperature independent, in contrast to U_b, S_b, and F_b. We wish to see what conditions allow S_b or U_b to dominate the free energy barrier, and also to gain some intuition about non-Arrhenius temperature dependence in general. Note that simulation times become nearly intractable when $\beta F_b = \beta U_b + S_b \gtrsim 10$, thus limiting how much of the growth of the barriers we can study.

Figure 2.11(a) shows data for the harmonic interaction potential for $R = 2.6$. As $R < 3$, the particles must overlap at $h = 0$ and thus $U_{\rm min} > 0$. The graph shows that as $T \to 0$, both βU_b and S_b grow. The growth of βU_b is more significant, pushed up by $\beta U_{\rm min}$. This situation is analogous to Model 2 from Sec. 2.3.3, where

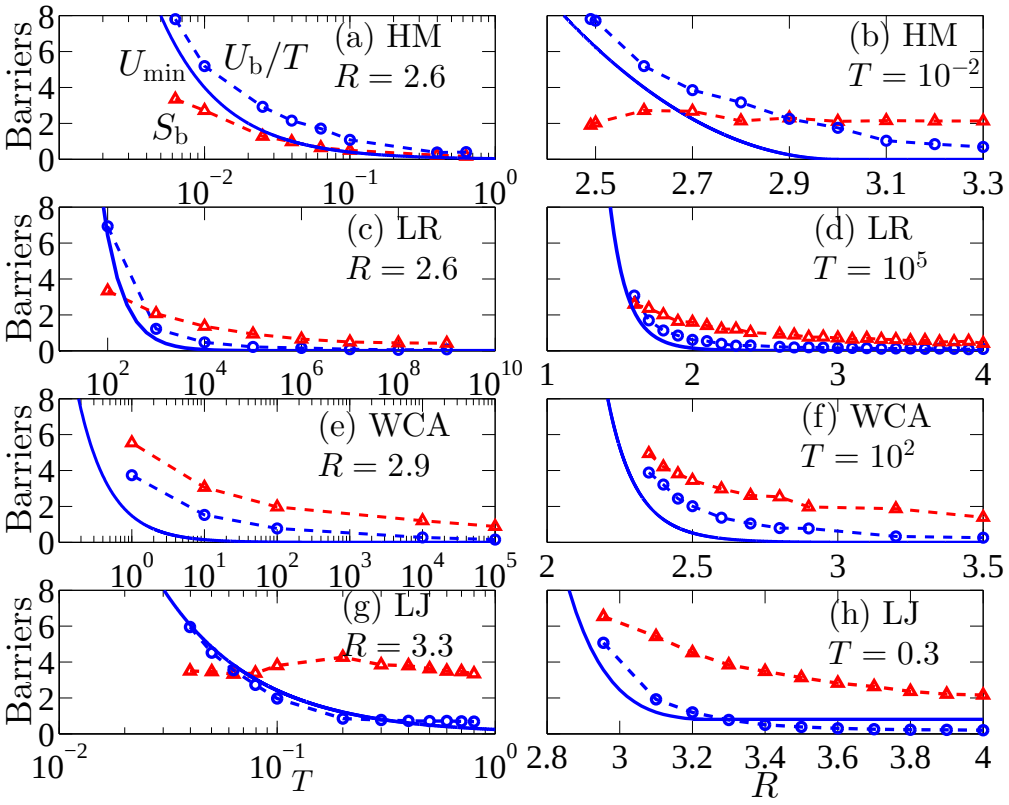

Figure 2.11: (Color online) Data for the potential energy barrier and entropy barrier for a variety of interaction potentials, temperatures, and system sizes R, as indicated. The solid curves indicate $U_{\min}$, the theoretical minimum potential energy barrier. The symbols indicate measured values (from the simulation data), connected by straight dashed lines. The meanings of the curves are all as labeled in (a). The interaction potentials are (a,b) harmonic ('HM'), (c,d) long-range ('LR'),(e,f) Weeks-Chandler-Andersen ('WCA') and (g,h) Lennard-Jones ('LJ').

$U_b \approx U_{\min} + \frac{1}{2}k_B T$ and $S_b \approx |\ln T|$. Given the slow growth of S_b, the free energy barrier is dominated by $U_{\min}$.

Figure 2.11(b) shows complementary data for the harmonic interaction potential as a function of R at fixed $T = 10^{-2}$. Given the finite range for the potential, $U_{\min} = 0$ for $R \geq 3$, although $U_b > 0$ as the particles overlap for some crossings. The $R > 3$ case is analogous to Model 3, whereas $R < 3$ is analogous to Model 2. The data in Fig. 2.11(b) show that entropy plays a smaller role for small R, where the free energy barrier is dominated by the potential energy. For this interaction potential, $U_{\min} \sim (R-3)^2$ for $R < 3$; the data show that S_b is nearly constant as a function of R.

Figure 2.11(c,d) shows the comparisons of entropic barrier and potential barrier for the LR potential. For large T or large R cases, $S_b > \beta U_b$. In the converse cases, the opposite is true. As the system becomes slower with a large free energy barrier, the free energy barrier is strongly determined by the potential energy component.

For the WCA data shown in Fig. 2.11(e,f), $U_{\min}$ goes to zero at $R = 3.245$, although as before we still have $\beta U_b > 0$. For the WCA potential, we see a more dramatic growth of U_b with decreasing T [panel (e)] and with decreasing R [panel (f)]. It appears that if we further shrink the system size in panel (f), U_b will eventually grow larger than S_b. The growth of S_b at small R is not as strong as the growth of $\beta U_{\min}$, and since $U_b > U_{\min}$, this further suggests that βU_b will be larger than S_b for smaller systems.

Figure 2.11(g,h) shows the comparisons of entropic barrier and potential barrier for the LJ potential. For high T cases [panel (g)], $S_b > \beta U_b$, with the opposite

occurring as $T \to 0$. Panel (h) shows that at a fixed T, with decreasing R both S_b and βU_b grow, with the latter growing more dramatically. It appears that if we further shrink the system size in panel (h), U_b will eventually grow larger than S_b.

Unusual behavior is seen for the LJ potential in Fig. 2.11(g,h), where $U_b < U_{\min}$ with large R and low T. This can be understood given the differences between our definitions of U_b and $U_{\min}$. U_{min} considers the difference in potential energy between the lowest potential energy path at the saddle point ($h = 0$) and the lowest potential energy the particles can obtain given R. The latter corresponds to a configuration where the centers of the particles form an equilateral triangle with side length = 2.24, corresponding to $h = 1.94$. However, this configuration is itself an unlikely configuration, and for example when $h = 1.94$ the three particles will often be in a configuration with slightly higher potential energy than the absolute minimum. This is essentially the same argument put forth in Sec. 2.3.3, that the average potential energy experienced by the system is not the minimum value. Thus, the *measured* potential energy difference U_b will often be between a slightly higher value for both $h = 0$ and $h = h_{\min}$, such that their difference $U_b = U(0) - U(h_{\min}) < U_{\min}$. This is not the case for the other interaction potentials, probably because the potential energy is a flatter function of h around $h_{\min}$ for the other interaction potentials.

Some general conclusions can be drawn from all of the data of Fig. 2.11. First, in most of the cases, $U_b > U_{\min}$, confirming the intuition from Sec. 2.3.3: that crossing the saddle point in the potential energy landscape is not typically done at the minimal potential energy path through that saddle point. Second, Fig. 2.11(a,c,e) demonstrates that βU_b and S_b both depend on T and are larger for colder tempera-

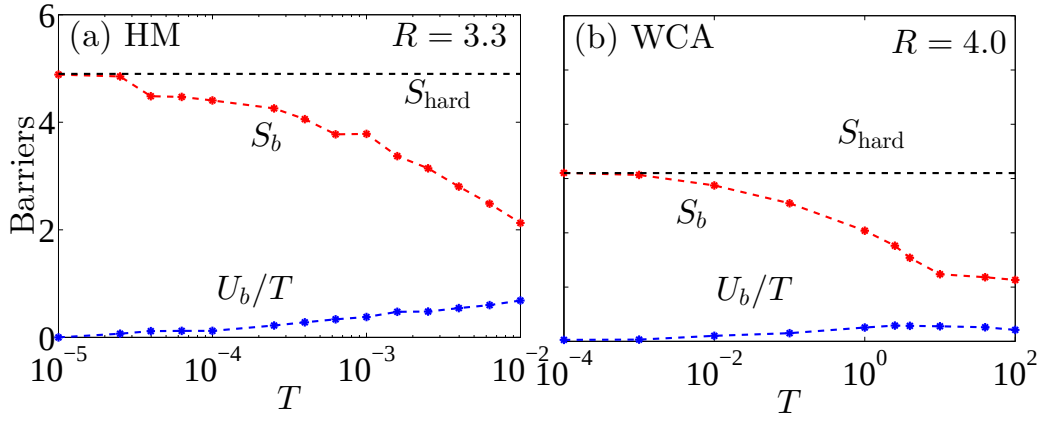

Figure 2.12: (Color online) The potential barrier and entropy barrier for (a) the harmonic interaction potential and (b) the WCA interaction potential. The system sizes R are as indicated, and chosen such that the minimum potential energy barrier is $U_{\text{min}} = 0$. The horizontal dashed lines indicate the free energy barrier for the hard disk case.

tures: and thus these barriers behave non-Arrheniusly. In particular, these barriers are not simply based on βU_{min}.

The finite-ranged potentials (harmonic and WCA) allow us to look at cases where $U_{\text{min}} = 0$. As noted in the discussion of Fig. 2.8(a,b), when $U_{\text{min}} = 0$ the free energy barriers reach a plateau as $T \to 0$ corresponding to the hard disk limit (the horizontal dashed lines). The data for the energy and entropy barriers are shown for two of these cases in Fig. 2.12. These data match the qualitative behavior predicted by Model 3 (Sec. 2.3.3). At low T, $\beta U_b \approx 0$ and S_b approaches the hard disk result. At high T, $\beta U_b \approx \frac{1}{2}$ and the entropic contribution decreases as more microstates are possible at $h = 0$. For different temperatures, the trade-off between crossing with zero or finite potential energy changes, due to the entropic penalty of choosing the zero potential energy pathway, which is weighted by the temperature.

2.4 Conclusions

We studied a free energy landscape of a simple model possessing some qualitative features of a glass transition. The model's slow dynamics are governed by a free energy barrier which we directly measure in simulations. The barrier height is determined both by entropy and potential energy. The relative contributions of each of these depend on temperature T. In particular, for fixed system size R, the potential energy landscape is independent of T, yet the effective potential energy barrier height, entropic barrier height, and overall free energy barrier all depend on T. This leads to non-Arrhenius temperature dependence. We conjecture that for cases with more particles, entropy plays an even more important role in cooperative rearrangements, as suggested in 1965 by Adam and Gibbs [25] and discussed by many authors subsequently. In fact, our model is quite in the spirit of Adam and Gibbs, in that rearrangements require coordinated motion of all three particles [Fig. 2.1(b)] which results in an entropic penalty.

There are qualitative differences between our model results and non-Arrhenius behavior seen in glass-forming systems. First, the onset of slow dynamics in our model requires temperature changes of several orders of magnitude (Fig. 2.8), whereas similar changes in glassy materials require a temperature decrease of only 10-20% [32–35, 56]. Second, in our model, as $T \to 0$, the potential energy component of the barrier may become more important than entropy, suggesting a possible recovery of Arrhenius behavior at the lowest T (Fig. 2.11). However, this is not completely clear from our data as the $T \to 0$ behavior requires prohibitively long simulation runs. Both of these differences between our simple model and glassy behavior might disappear for

larger numbers of particles, but then we would lose the ability to fully visualize the free energy landscape (Fig. 2.3). It is certainly known that near the glass transition, rearrangements can involve far more than three particles [52, 53], which would likely enhance the sensitivity to temperature. While we do not provide a realistic description of the $N \to \infty$ limit of a glass transition, we have demonstrated connections between the free energy landscape, free energy barriers, and non-Arrhenius temperature dependence in our model glassy system.

Chapter 3

Extensions of three-disk model

3.1 Mapping particles with soft interaction potentials onto hard particles with an effective size

The comparison between Hunter's hard-disk model [51] and the soft-disk model described in Chapter 2 leads us to a question: whether there is a way to map particles with soft interaction potentials onto hard particles with some effective size. The idea of using hard particles to approximate soft particles has a long history (see the discussion in Ref. [62]), and has been applied to questions related to liquids [60] and glasses [55]. For our three particle system, the hard disk case has been described in detail in Ref. [51]. A key result of that work is that the free energy barrier grows as $F_b \sim \ln(R-3)^{-7/2}$ as $R \to 3$, due to an entropic barrier which can be calculated analytically. The calculation will be demonstrated in detail in Chap. 3.2. Figure 3.1 shows the result of Hunter's work: free energy barrier grows as $\ln[(R-3)^{-7/2}]$ as

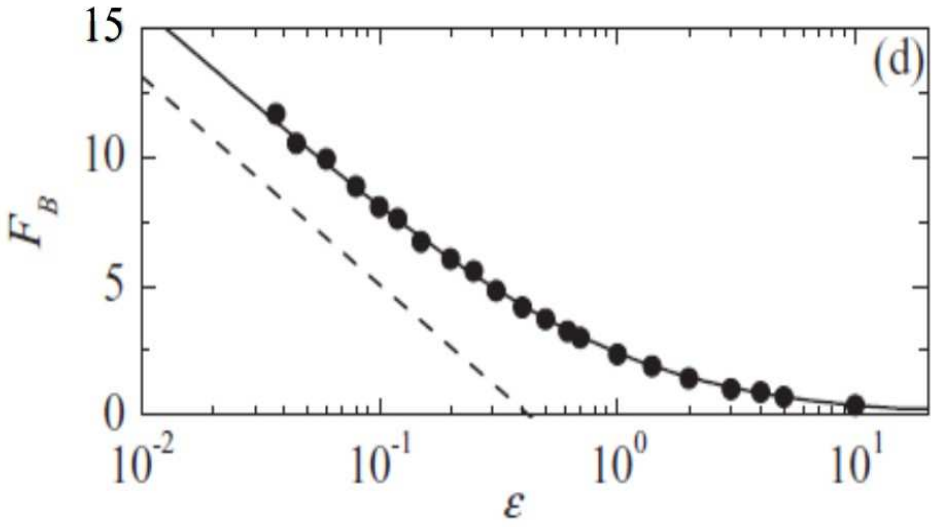

Figure 3.1: Free energy barrier, which in hard-disk system is entropy barrier, as a function of ϵ ($\epsilon = R - 3$). Circles are simulation results and dashed line grows as $\ln[\epsilon^{-7/2}]$. The solid line comes from calculation. Reprinted by permission from [51]. License Number: 3902791310106

$R \to 0$.

Due to the softness of soft particles, they are deformable with some compensation of potential energy. For particles with finite-range potential energy, more overlap leads to larger potential energy compensation. Two soft particles can squeeze all the way down together until thermal energy could not support the potential energy compensation. As is shown in Fig. 3.2, the soft particles could be considered as two hard particles with smaller effective radius which is represented as the dashed circles.

The effective hard particle size must depend on both the interaction potential and the temperature. While there are several methods for finding an effective hard particle size [62], we find only one method that works for our simulations, and even that is limited to only some conditions. We set an effective hard sphere radius r_{eff} such

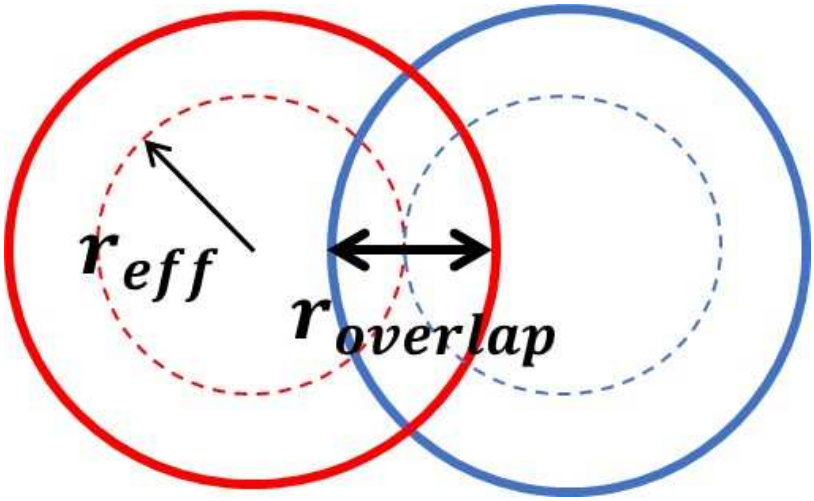

Figure 3.2: The sketch of effective radius of soft particles. Solid circles are the real size of two soft particles. $r_{overlap}$ is the overlapped distance between the two particles. Dashed circles represent the effective hard particles.

that the inter-particle repulsive energy at this center-to-center separation between two particles is equal to the thermal energy:

$$U(r_{ij} = 2r_{eff}) = k_B T. \tag{3.1}$$

For situations such as the harmonic potential where particles have a soft interaction with the confining wall, we also redefine the system size R' along similar lines.

This method works for the finite-range potentials (harmonic and WCA) and only for original system sizes $R > 3$(HM) and $R > 3.24$(WCA), as shown by the data collapse in Fig. 3.3. The meaning of this is that these soft particles can be approximated as particles which can come together with pair-wise interaction energy up to $k_B T$ easily, and no closer. However, Eqn. 3.1 fails to collapse the data for $R < 3$, where the particles are required to have potential energy $U_{\min} > 0$ to be in the transition state ($h = 0$). In these situations, the free energy barrier has a potential energy

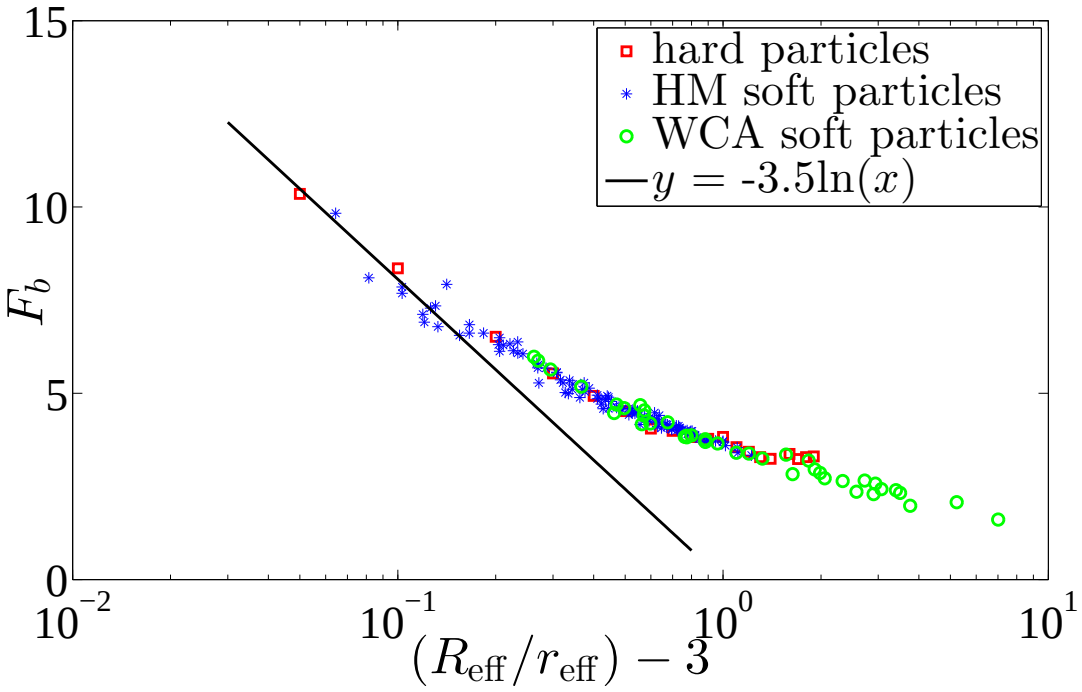

Figure 3.3: The free energy barrier F_b plotted as a function of $(R'/r_{\rm eff}) - 3$. For hard particles with $r = 1$, the free energy barrier scales as $\ln(R-3)^{-7/2}$ for $R \to 3$ as shown by the line [51]. In this figure, R ranges from 3.0 to 4.0 for both HM and WCA systems. And T ranges from $10^{-4.8}$ to 10^{-2} for HM systems. T ranges from 10^{-4} to 10^{4} for WCA systems.

contribution from $U_{\min}$ which cannot be easily approximated by an entropic contribution due to hard particles. Once the particles are at $h = 0$ with energy $U_{\min}$, they could potentially be thought of as having an extra $k_B T$ of energy to explore the $h = 0$ state with some effective hard particle size, but this depends in a complicated way on the interaction potential of all three particles, and cannot be treated in a pair-wise fashion such as Eqn. 3.1 tries to do. While one could always determine a hard particle size that gives the same F_b as the soft particle, there is no simple scheme to do so such as Eqn. 3.1 or other methods discussed in [62]. The long-range potentials such as LJ and the $1/r^{12}$ potential suffer from similar problems, that there is no simple pairwise method for finding a hard particle size, as interactions between all three particles (and the wall as well) always matter.

3.2 Entropic Barrier for Hard Disks

As mentioned in Chap. 3, some of the simulation results could be calculated analytically, such as the entropy barrier for hard-disk system. This section demonstrates the details of the calculation procedure.

We calculate the entropy of a system with a number of particles based on the canonical ensemble,

$$S_b = -\ln \Omega, \tag{3.2}$$

where Ω is the sum of probability of each state with specific position and specific momentum at the crossing state. In hard-disk system, the probability at each state is the same. At crossing state, the degree of freedom in the system could be reduced from 6 to 4 as is shown in Fig. 3.4. We define x_1, x_2 and x_3 as the distance between

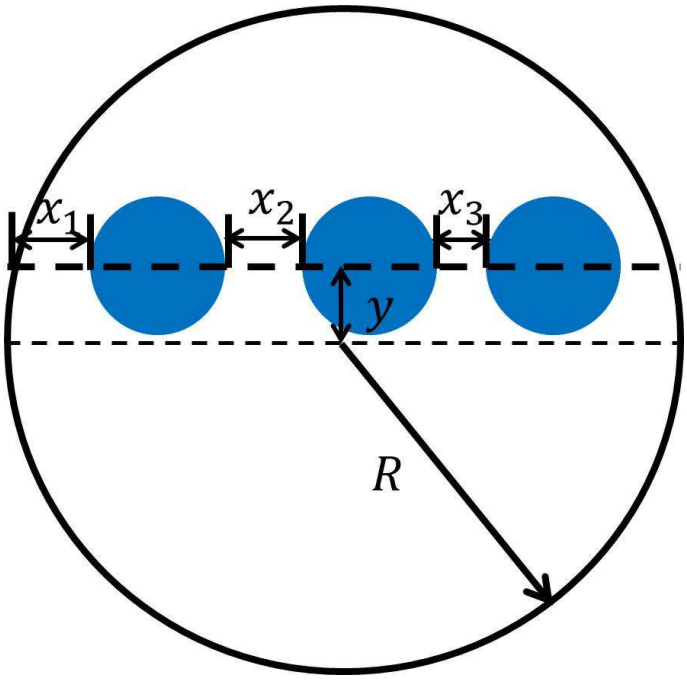

Figure 3.4: The sketch of the definition of three degrees of freedom in x-axis.

disks and the wall of the edge of the circular cage. And the system has one degree of freedom in y-axis. The distance between the third disk (the right-most disk in Fig. 3.4) and the edge of the circular cage can be calculated with x_1, x_2, x_3 and y. In this way, the system at crossing state has 4 degrees of freedom. To simplify the derivation process, we define the spare length on the diameter of the cage when all of the three hard disks locate on the diameter as $\varepsilon = 3 - R$. So the multiplicity can be derived as follows,

$$\begin{aligned}
\Omega(\varepsilon) &= \int_0^{\varepsilon} dx_1 \int_0^{\varepsilon - x_1} dx_2 \int_0^{\varepsilon - x_1 - x_2} dx_3 \int_{-\sqrt{\varepsilon^2+4\varepsilon}}^{\sqrt{\varepsilon^2+4\varepsilon}} dy \\
&= 2\sqrt{\varepsilon^2+4\varepsilon} \int_0^{\varepsilon} dx_1 \int_0^{\varepsilon - x_1} (\varepsilon - x_1 - x_2) dx_2 \\
&= \sqrt{\varepsilon^2+4\varepsilon} \int_0^{\varepsilon} (x_1 - \varepsilon)^2 dx_1 \\
&= \frac{\sqrt{\varepsilon^2+4\varepsilon}}{3} \varepsilon^3 \\
&\sim \varepsilon^{3.5} \qquad\qquad (\varepsilon \ll \varepsilon^2 \ \text{ as } \ \varepsilon \to 0).
\end{aligned}$$

According to Eq.3.2, the entropy barrier at crossing state is $S_b = \ln(R-3)^{(-7/2)}$ as $R \to 0$, which is consistent with the simulation result.

In soft-disk system, the probability for the disks at each state are not the same and it follows a Boltzmann distribution, $P(x_1, x_2, x_3) = e^{-\beta U(x_1, x_2, x_3)}$. And the derivation becomes very tedious and we would not demonstrate it in this draft.

3.3 Apply Forward Flux Sampling to Glassy Model System

Due to the long time scale for a glassy system transiting between two inherent structures or metastable states, one important problem in computational research on glass transition is to calculate the rate of rare events within a feasible computing time. In this chapter, we introduce forward flux sampling as a good method to solve the problem of long time scale in computational research on glassy systems.

3.3.1 Forward Flux Sampling

Forward flux sampling (FFS) method is a convenient and efficient computational method for calculating rate constants of rare events in both equilibrium and non-equilibrium systems [63–65]. This method generates the rare events trajectories between two steady states A and B in a ratchet-like manner as is shown in Fig. 3.5 [66]. A and B are regions in the configuration space. The regions in the configuration space is represented as $\lambda(x)$, where x is the coordinate of the configuration space. In this way, the system is in region A if $\lambda(x) \leq \lambda_A$ and in region B if $\lambda(x) \geq \lambda_B$. As is shown in Fig. 3.5, between regions A and B, we define a sequence of non-overlapping interfaces $\{\lambda_1, \cdots, \lambda_n\}$, such that $\lambda_1 \geq \lambda_A$ and $\lambda_n \leq \lambda_B$ [66]. A trajectory evolving from A to B has to cross each interface at least once. The rate constant k_{AB} for transitions from A to B is given by

$$k_{AB} = \Phi_{A,1} \prod_{i=1}^{n} P(\lambda_{i+1}|\lambda_i). \tag{3.4}$$

Here, $\Phi_{A,1}$ is the rate for the system transiting from region A to interface λ_1. And $P(\lambda_{i+1}|\lambda_i)$ is the probability that the system comes from A and crosses λ_i for the first time and will reach λ_{i+1} before returning to A. Thus, the flux from A to B is the flux from A to λ_1, multiplied by the probability for a trajectory reaching each successive interface from the previous one and eventually arriving at B without returning to A (which could be presented as $P(\lambda_B|\lambda_1) = \prod_{i=1}^{n-1} P(\lambda_{i+1}|\lambda_i) \times P(\lambda_B|\lambda_n)$). The flux of trajectories leaving from A and reaching at B is k_{AB} and the time scale for the system transiting from stable state A to stable state B is $\tau = 1/k_{AB}$, which is what we care about in a glassy system.

Forward flux sample method dramatically decreases the computational time for the transition between two stable states because it simulates the trajectories in a rachet-like manner instead of a brute-force manner. Forward flux sampling method decomposes the configuration coordinate into a series of interfaces to break the problem down into a series of smaller steps. The probability of making these smaller steps is much larger than that of the complete transition from A to B. In this way, we are simulating a bunch of high probable events instead of simulating one extremely small probable event. And the number of high probable events is the number of interfaces placed in the configuration space, which is much smaller compared with the waiting time of the extremely rare event.

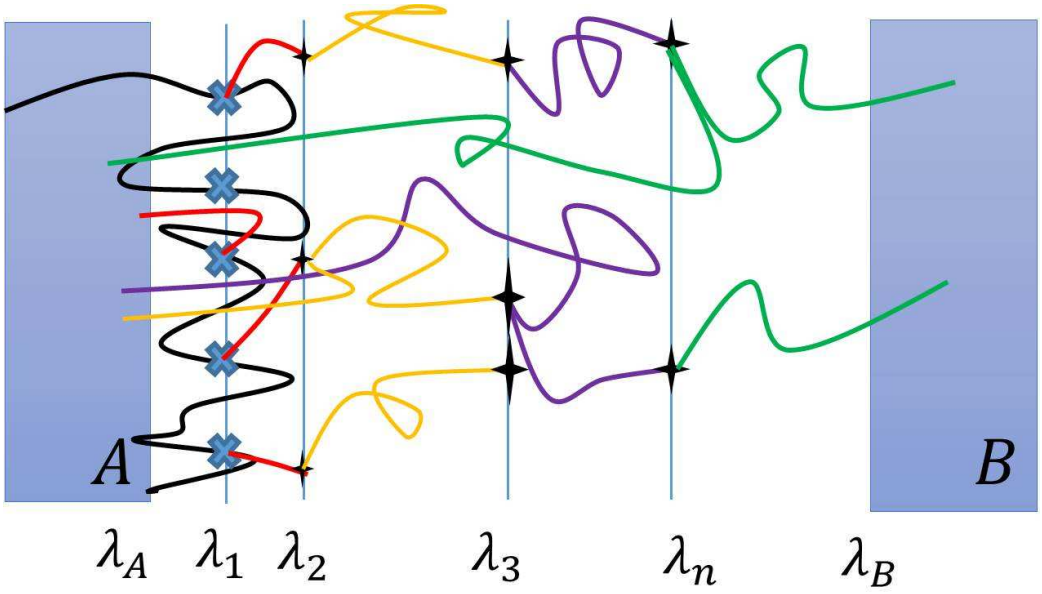

Figure 3.5: The sketch for forward flux sampling algorithm. The interfaces λ_i partition the configuration space between A and B into adjacent regions. In the first stage of a forward flux sampling simulation, one runs a trajectory starting in stable state A. Each time the trajectory exits region A and successively crosses interface λ_1, the system configuration is stored, as indicated by the crosses on the line of λ_1. And then the simulations restart from randomly chosen (previously stored) configurations at λ_1. Each simulation is terminated when the trajectory crosses the next interface, λ_2, or returns to A. This procedure is repeated at each interface until it reaches λ_n.

3.3.2 Optimized Interface Placement in Forward Flux Sampling

The positions of interfaces between two stable states strongly influence the efficiency of forward flux sampling. In this section, we introduce the method which optimizes the interface placement and improves the efficiency of the computation [67]. The general idea of the optimized forward flux sampling is that placing more interfaces in the bottleneck regions where the crossing probability is low and placing fewer interfaces in the easy-crossing regions.

The computational efficiency of a forward flux sampling calculation is 1 over the product of the statistical error and computational cost [68],

$$\varepsilon = \frac{1}{\zeta\nu}. \tag{3.5}$$

The computational cost, ζ, is proportional to the number of interfaces and some computational constants. The statistical error of the estimated rate constant is

$$\nu \approx \sum_{i=0}^{n-1} \frac{(1-p_i)}{M_i p_i}, \tag{3.6}$$

where M_i is the number of trial trajectories and p_i is the probability of trajectory reaching interface i [69]. According the Eq. 3.6, the statistical error is minimized when $M_i p_i$ is the same for all the interfaces [67]. In other word, when the net flux of trajectories is the same for each interface, the system has the smallest statistical error. Based on the previous theoretical analysis, practically we fire the same number of trajectories for each interface ($M_i = M = const$) in the simulation. Then, we place the interfaces at the positions with a same probability, p_i. And according to

Kratzer's work in 2013 [67], placing the interfaces where the success probability p is in the range of $[0.3, 0.7]$ should generally result in a high computational efficiency.

3.3.3 Applying Forward Flux Sampling to Glassy Model System

We apply the forward flux sampling with optimized interface placement to the soft three-disk model which is introduced in Chap. 2. This method allows us to simulate the transition event with the time scale as large as 10^{50} within reasonable computational steps.

In three-disk model, the configuration coordinate is h. The time scale is 1/flux, which is $1/P_{A|B}$. And we set stable state A as the region where $h \leq -1$ and state B as the region where $h \geq 1$. According to the theoretical analysis in Chap. 3.3.2, the interfaces are placed between $h = -1$ and $h = 1$ with the same net flux of trajectories, p_i, for each interface. And in our forward flux sampling simulations, we choose $p = 0.3$, which satisfies the optimal conditions mentioned in Chap. 3.3.2. Figure 3.6 shows the time scale, τ, for rearranging events in a system with harmonic potential as described in Chap. 2.3 as a function of confinement size. Since the typical time scale at glassy state is 10^{15} times greater than diffusion time scale (the time a free particle would take on average to diffuse a distance of 1), the graphs only shows the time scale in the range of $[10^5, 10^{20}]$. Actually, using the forward flux sampling methods, we can simulate the transition event with the time scale as high as 10^{50} times greater than the diffusion time. The life time diverges at low temperature regimes with small confinement sizes.

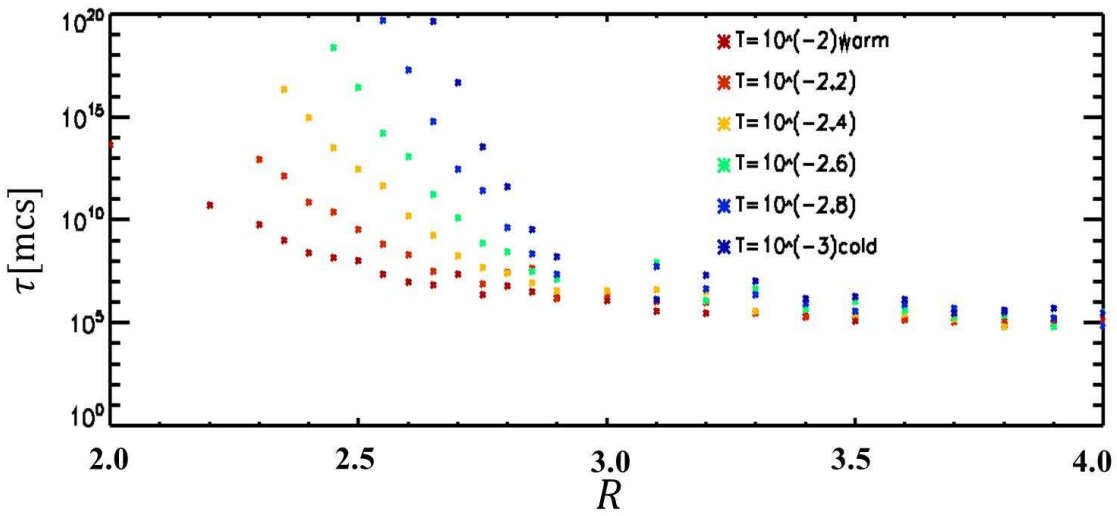

Figure 3.6: Time scale, τ, calculated using forward flux sampling method in a harmonic potential model system. y-axis is the time scale in Monte Carlo steps for a transition event in soft three-disk model with harmonic potential energy. x-axis is the radius of the circular confinement. Each star in the graph represents the time scale for the system with specific temperature and confinement size. Different colors denote different temperature ranging from 0.01(red) to 0.001(blue). Since the typical time scale at glassy state is 10^{15} times greater than warm and dilute diffusion time scale, the graphs only shows the time scale in the range of $[10^5, 10^{20}]$. The time scale grows dramatically at low temperature and in small confinement.

Since the forward flux sampling method can simulate the cooperative rearrangements with dramatically large time scale in our simple model, it can provide us interesting results that verify several conjectures based on the theoretical analysis for simple models in Chap. 2. In Chap. 2, we show a non-Arrhenius temperature dependence of the time scale and conjecture that the time scale at least grows proportional to $\exp(-\beta U_{\min})$. As defined in Chap. 2, $U_{\min}$ is the minimum potential energy needed to cross $h = 0$ when the system finds the optimum transition path and it is temperature independent. $U_{\min}$ is independent on T. As the size of the model system decreases, $U_{\min}$ increases and the time scale increases exponentially. The dramatic increase of the time scale makes it impossible to simulate the rearrangement within a reasonable computation time using traditional brute-force methods. Figure. 3.7 is a graph of the time scale of rearrangement, $\ln \tau$, in function of $\beta U_{\min}$. The data in this graph are generated using forward flux sampling method for the harmonic potential model with confinement size smaller than 3 and $U_{\min} > 0$. It shows the linear relationship between $\ln \tau$ and the minimum potential energy, $\beta U_{\min}$, which is consistent with our the theoretical analysis of transition time scale for simple model 3,

$$\tau = \tau_0 \exp(\beta U_{\min}) \exp(\beta F), \tag{3.7}$$

where $U_{\min}$ is the minimum potential energy to transit with the optimum transition path and F is the additional free energy barrier which provides additional non-Arrhenius scaling as F grows with T.

We calculated the non-Arrhenius component of the free energy barrier, βF, based on Eqn. 3.7 since $U_{\min}$ is constant with a certain confinement size. As the system approaches glass transition, the potential energy barrier approaches $U_{\min}$, so the non-

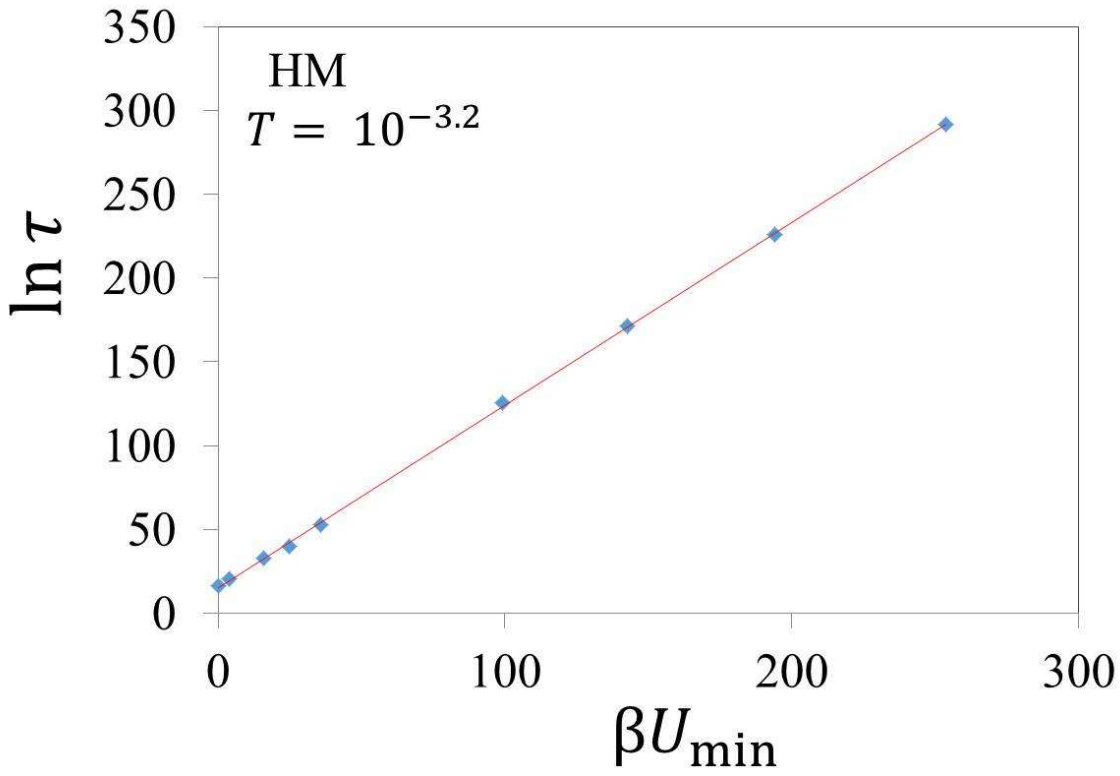

Figure 3.7: The transition time scale of a harmonic potential system in function of $\beta U_{\min}$. The y-axis is logarithm. In this system, $T = 10^{-3.2}$ and R ranges from 2.2 to 3.0. The red line is a linear fitting for the data generated with forward flux sampling method. The linear fitting indicates that τ is proportional to $\exp(\beta U_{\min})$ and $\beta U_{\min}$ is the Arrhenius contribution for the time scale.

Arrhenius component approximately equals to the entropy barrier, S_b. For the simple model 2 demonstrated in Chap. 2.3.3, the system only crosses at $|x| \lesssim \sqrt{k_B T/U_0}$ at low temperatures. By calculating the number of configurations at the transition state, we can compute the entropy barrier based on the canonical ensemble (Eqn. 3.2) and the result shows that entropy barrier grows in proportional to $|\ln T|$. Figure. 3.8 shows that the entropy barrier grows with decreasing T and follows the relation as $\beta S_b \sim |\ln T|$ as the system approaches glass transition. This computational result is consistent with our theoretical anticipation in Chap. 2.3.3 for model 2. In summary, in the model interacting with harmonic potential energy, the potential energy barrier is independent on T and the entropy barrier follows the relation as $\beta S_b \sim |\ln T|$ when the system approaches glass transition.

Forward flux sampling method works well in our soft three-disk model and it successfully provides the information of the transition events at low temperature and small confinement regime when the system is approaching the glass transition. The forward flux sampling provides us a potential computational algorithm to study the long-time-scale events in glassy system which is infeasible using the traditional brute-force method.

3.4 Conclusion

In this chapter, we introduce some extended studies on jamming transition of the soft three-disk model. Since soft particles are deformable with some compensation of potential energy, they could be considered as a hard particle with a smaller effective size. We find a way to map particles with soft interaction potentials onto hard

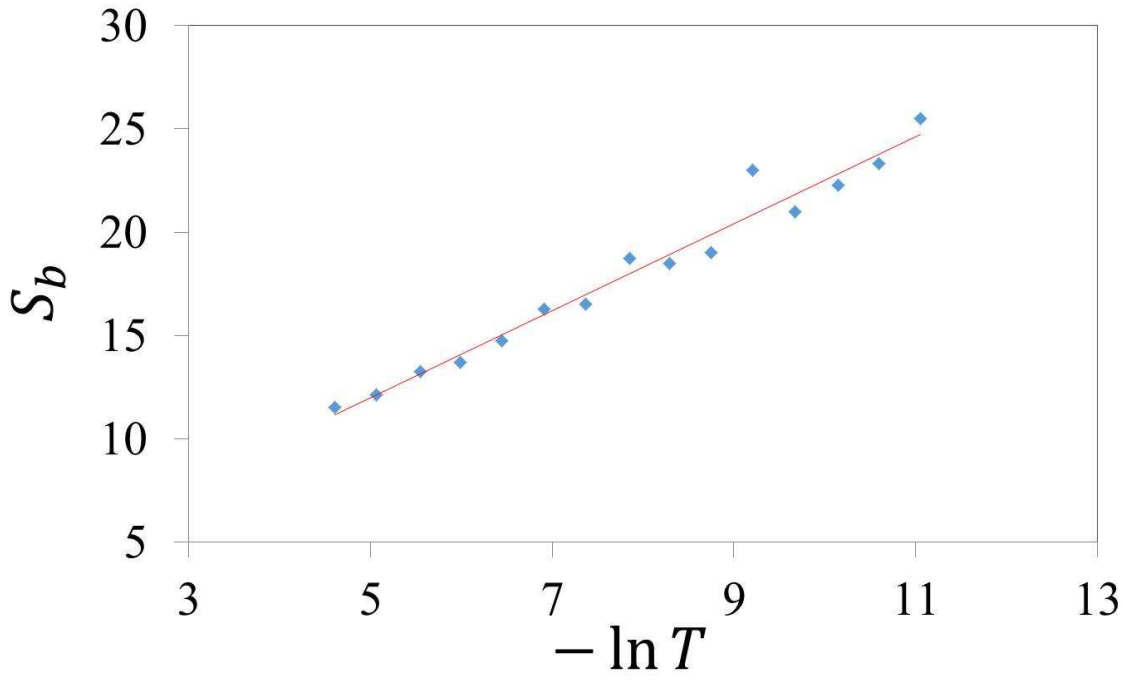

Figure 3.8: The y-axis is the entropic component of the energy barrier, βS_b, when $T \to 0$. The x-axis is the logarithm T. The red line is the linear fitting for the data generated by forward flux sampling method for harmonic potential model. As $T \to 0$, $\beta S_b \sim |\ln T|$.

particles with some effective size by treating the particles in a pair-wise fashion. And this method works for the finite-range potentials (harmonic and WCA) and only for original system sizes $R > 3$ (HM) and $R > 3.24$ (WCA). It does not work for system with small confinement due to the high entropy compensate to reach the theoretic minimum potential energy, $U_{\min}$.

To develop the simulation method for glassy system, we introduce forward flux sampling as a convenient and efficient method to calculate long time scale for the transition between two inherent structures. It successfully provides the information of the transition events at low temperature and small confinement regime which is infeasible using the traditional brute-force method. The computational data generated with forward flux sampling method show that the transition time scale for our simple model grows proportional to $\exp(-\beta U_{\min})$, which gives an Arrhenius scaling with T. The time scale can be expressed as $\tau = \tau_0 \exp(\beta U_{\min}) \exp(\beta F)$. The additional free energy barrier βF associated with the $h = 0$ potential energy landscape cross-section grows with decreasing T and as $T \to 0$, $\beta F \sim |\ln T|$. The computational results are consistent with our anticipation in Chap. 2.

Chapter 4

Rearrangements During Slow Compression of a Jammed 2-D Emulsion

4.1 Introduction

Amorphous materials including foams, emulsions, colloidal suspensions and granular materials can jam into a rigid, disordered states [70]. The slowly compressed systems of non-Brownian soft particles interacting through repulsive contact forces are typical models for understanding jamming transition because they provide a sufficiently completed jamming process. With enforced packing fraction in the systems, the contact forces grow, the deformation of the soft particles increases and they exhibit rich geometrical and mechanical properties. Some recent studies reveal that the geometrical and mechanical properties are strongly correlated [14]. During the

jamming process, both heterogeneous particle rearrangements and the heterogeneous local structures are observed in experimental and computational research [71–75]. To study the correlation between the heterogeneous local dynamics and the structural heterogeneities, characterizing the structural inhomogeneity is an essential problem in understanding amorphous materials. Free volume is a simple and basic measurable parameter for characterizing the local structure in amorphous materials [76–78]: rearrangements easily occur in regions with large free volume. However, this concept only applies at packing fractions below jamming [1]. A new analysis method based on the radical Voronoi cells proposed by Rieser in 2015 shed a light on characterizing the local structure in amorphous materials [1].

In this chapter, inspired Bolton's foam model [14], we study the jamming process of a emulsion system as water slowly evaporates in experiments. In our system, the emulsion droplets are non-Brownian and interact with the neighbor droplets by repulsive contact forces. And we characterize the heterogeneity of the local structure based on radical Voronoi cells, which is proposed by Rieser and Durian [1]. And we analyze and demonstrate the strong correlation between the geometrical properties and the dynamics properties in the slowly compressed emulsion system.

4.2 Experiment

Our emulsions are silicon oil droplets in water using Fairy detergent (mass fraction 0.025) as a surfactant and are produced with the 'co-flow' microfluidics technique [79]. The radius polydispersity of our droplets generated with this technique is 1%. To avoid crystallization, we make a binary sized emulsion system by mixing two batches

of monodisperse droplets at a volume ratio of about 1:1. We create a chamber with two 25 mm × 75 mm glass slides separated by pieces of $100\mu m$ transparency film sealed with epoxy. These pieces of film create a gap of $120\mu m$ between the slides. Also, the film creates in a circular space with two small opening edges in the chamber. Figure 4.1 shows the sample chamber used in our experiment. In the experiment, the droplets are confined between the two glass slides. The diameters of the droplets are larger than the gap of the sample chamber. Thus, the droplets are squeezed between the two glass slides without overlapping and form a quasi-2D system. Figure 4.2 is a sketch of the side view of the quasi-2D emulsion samples. The droplets are deformed into a pancake shape which are denoted as blue ellipse. In experiment, the two dimensional diameter ratio of the two batches of droplets is about 1.5:1. The mean 2-D diameters of the large droplets and the small droplets are 379 μm and 265 μm.

In the experiment, the chamber filled with emulsion droplets stays on the microscope for 3-5 hours. As water slowly evaporates from the two opening edges of the chamber as is shown in Fig. 4.1, the area fraction of the system gradually increases. We image the droplets with a 5× objective on an inverted microscope, using a 20 frames per second camera to take a video of the droplets' motion. In our experimental system, the time interval between each frame is 30 s. During this process, we observed many rearrangement events occurring. The calibration of this image is 211 pixel equivalent to $1000\mu m$. We did not observe net migration of the droplets in the video, so the imperfection in the parallelity of the pair of glass slides is apparently negligible. Figure 4.3 shows the first and last pictures of the experimental system. At the beginning of this compressing process, the droplets are randomly close packed but

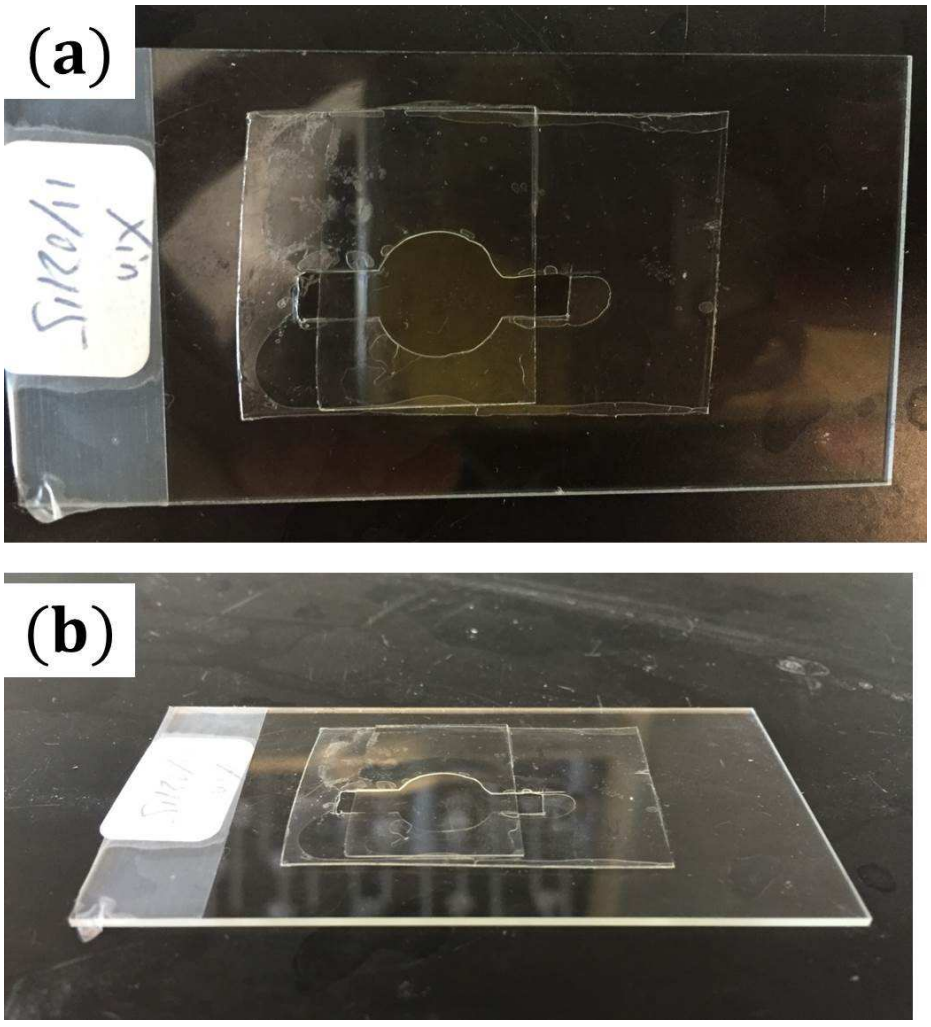

Figure 4.1: (a) Top view and (b) side view of the sample chamber. Water gradually evaporates from the two open edges. The length of the glass slides is $7.5cm$.

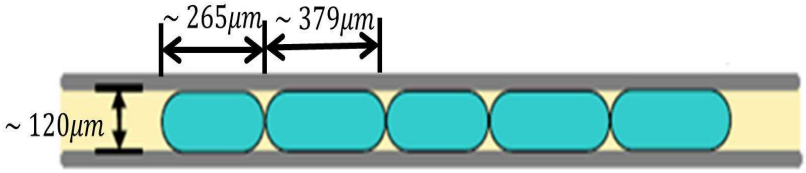

Figure 4.2: The side view of the chamber and emulsion sample. Droplets (shown in blue) are squeezed between two glass slides and deformed into a pancake shape. The gap thickness is typically about $120\mu m$. The sketch shows bidisperse sample with two typical diameters of droplets $265\mu m$ and $379\mu m$.

barely deformed as is shown in Fig. 4.3(a). In the end of this process in Fig. 4.3(b), the emulsion droplets all deform into non-circular shape, some of which are close to polygons. As the evaporation occurs, to fill in the void space and get close to their neighbors, the droplets exhibit local rearrangement with their neighbors. Some research work on jamming of soft materials indicate that the geometric and mechanical response are correlated [2, 14]. In this chapter, we would answer the question: which droplets are going to rearrange? To answer this question, we use the method proposed by Rieser and Durian [1], characterizing the local structure of amorphous materials based on the radical Voronoi network.

4.3 Method of Voronoi Vector Field

To figure out which droplets are going to rearrange, we characterize the local structural heterogeneity based on the radical Voronoi tessellation. Voronoi tessellation is a partition of the plane into many polygon cells, one for each point on the plane. The radical tessellation keeps main topological features of the ordinary Voronoi tessellation

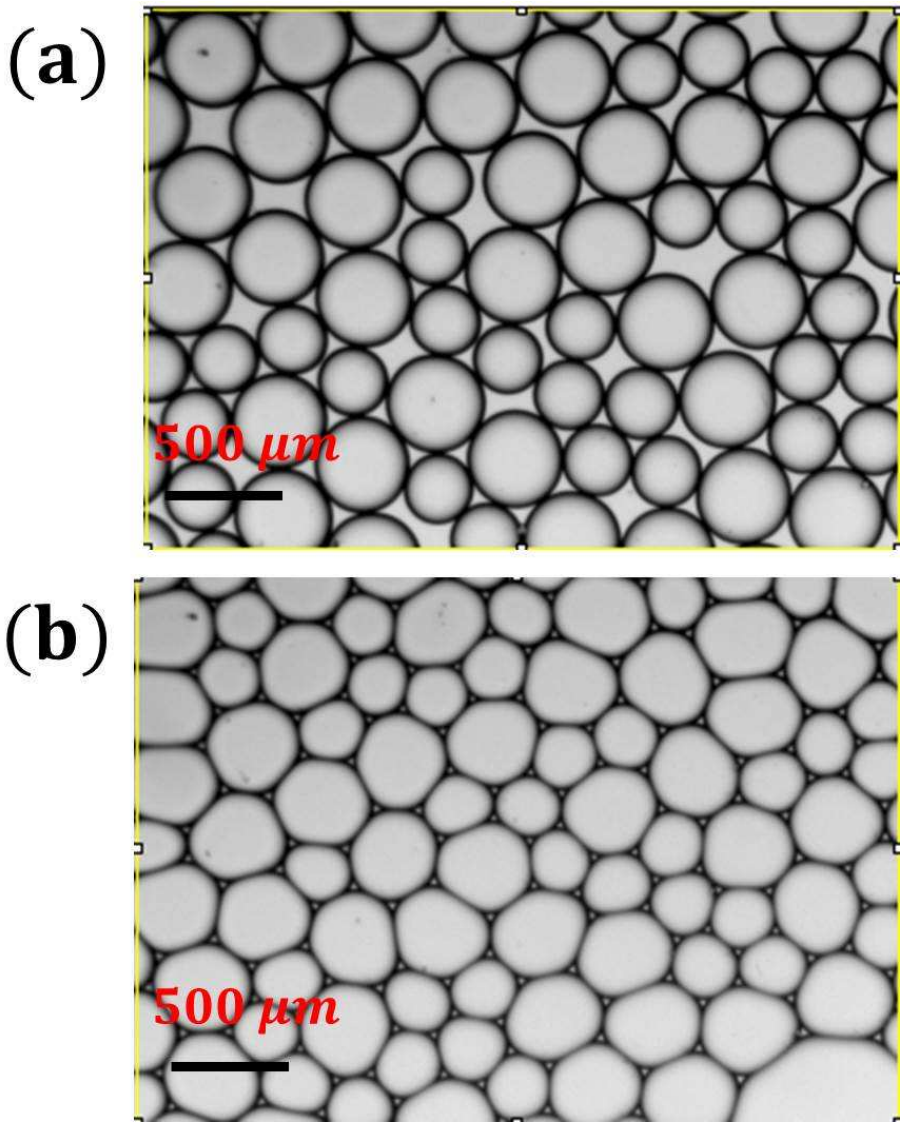

Figure 4.3: The photographs of the quasi-2D emulsion system. It is a binary-sized system. (a) The first image at $t = 0hr$ with $\phi = 0.86$. (b) The last image at $t = 2hr$ with $\phi = 0.98$.

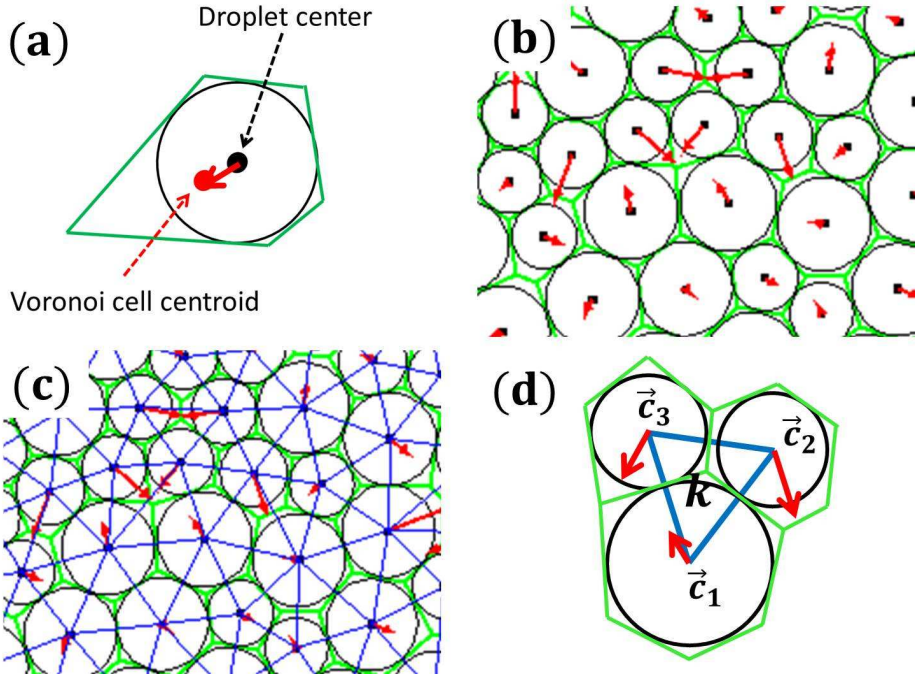

Figure 4.4: (a) The green polygon is the radical Voronoi cell for the droplet. The black dot is the droplet center and the red dot is the radical Voronoi cell center. Typically, these two centers are not overlapped. The Voronoi vector is shown as the red arrow which points from the particle center to the Voronoi cell center. (b) The Voronoi vector field is demonstrated by the red arrows for each droplet. (c) The Voronoi vector field with Delaunay triangulation (blue). (d) The example of one Delaunay triangulation with three corresponding droplets and the Voronoi vectors. In (b),(c) and (d), in order to make the red arrows visible, we magnified the length of the vectors by 30 times.

and is well adapted to granular systems with unequal spheres or disks. It subdivides the space into polygon cells according to the radical axis for each pair of droplets and each droplet resides in one cell. The sides of the radical Voronoi polygons are on the radical axis for each pair of droplets. As is shown in Fig. 4.4(a), we assign one radical Voronoi cell to each droplet which is the green polygon in the picture. Typically, the droplet's center and the Voronoi cell centroid are not the same. If we create a vector points from the droplet center to the Voronoi cell centroid, we've got a vector that approximately pointing towards the free space within the corresponding Voronoi cell. This vector is defined as the 'Voronoi vector', $\vec{c}$ [1]. In our experiment, the area fraction of the emulsion system, ϕ, slowly increases and the droplets need to fill in the void space to get closer to the neighbor droplets. So we anticipate that the direction of Voronoi vector indicates the direction of droplet displacement. Each droplet has its corresponding Voronoi vector and these vectors form a vector field. We use $\vec{\mathbf{c}}$ to represent the Voronoi vector for each droplet. And we could calculate the local divergence of this vector field [1] based on Delaunay trianglulation. Delaunay triangulation is a group of triangles in a plane with a set of points as the vertices such that no point is inside the circumcircle of any triangle and the minimum angle of all the angles of the triangles is maximized to avoid sliver triangles. In our system, the plane with a set of points is the 2-D plane with a bunch of droplets' centers. As is shown in Fig. 4.4(c) and(d), we perform interpolation and differentiation of the vectors over Delaunay triangulations as the local regions. The divergence of a field is defined by interpolating the vectors over the local region of each Delaunay triangle,

k. Then, we define the divergence for each triangle, D_k, as

$$D_k = \vec{\nabla} \cdot \vec{\mathbf{c}}. \tag{4.1}$$

And then we apply the framework of the constant strain triangle of finite element analysis to find local spatial variations of the vectors [80]. The Voronoi vector has $\mathbf{c}$ has x and y component as $\mathbf{c} = (c_x, c_y)$. And for each triangle, c_x and c_y can be expressed as a strain matrix:

$$c_x(x, y) = d_x + d_{xx}x + d_{xy}y, \tag{4.2}$$

$$c_y(x, y) = d_y + d_{yx}x + d_{yy}y. \tag{4.3}$$

For each Delaunay triangle, the constants d_x, d_y, d_{xx}, d_{xy}, d_{yx} and d_{yy}, are determined by three pairs of Eq.4.3 corresponding to the triangle vertices. We measure the Voronoi vectors, $\vec{\mathbf{c}}$. And by evaluating and inverting the resulting matrix equation, we can calculate d_x, d_y, d_{xx}, d_{xy}, d_{yx} and d_{yy}. The local divergence is given by $Tr(d_{ij})$, where the tensor $d_{ij} = \partial c_i / \partial x_j$. The regions with $D_k > 0$ are more tightly packed than their surroundings and could be called overpacked regions. The regions with $D_k < 0$ are less tightly packed than their surroundings and are considered underpacked regions. As the system slowly compressed, we anticipate that rearrangements should occur to move droplets away from the overpacked regions and towards the underpacked regions. In this chapter, we study the correlation between rearrangements and the Voronoi cell vector field.

4.4 The Directionality of Droplets Motion

We find a correlation between the Voronoi vector and the droplet displacement. In experiment, the time interval between each frame of the video is $30s$. The time interval for displacement discussed in this chapter is $30s$. As is mentioned in Chap. 4.3, the Voronoi Vector indicates the direction of the void space surrounding the corresponding droplet. As water slowly evaporating and the system getting crowded, the droplets need to fill in the void space and get close to each other. In this way, it is reasonable to assume that the direction of the Voronoi vector somehow indicates the direction of droplets motion. As is shown in Fig. 4.5, the Voronoi vectors within the red square window point towards the void space and we anticipate that those droplets are going to move towards the void space as the system is slowly compressed. Figure 4.6 defines the angle θ between the direction of Voronoi vector and the direction of displacement. Our assumption is that θ should be close to $0°$. However, the experimental result doesn't agree with our assumption. Figure 4.7 is the histogram of the angle θ of all the particles through out the whole compressing process. The curve peaks at $0°$ and $180°$, which correspond to the droplets moving towards the Voronoi vector direction or go to the opposite direction. This behavior doesn't consist with our anticipation. In order to understand this puzzling behavior, we looked into the details of one typical rearrangement example, as is shown in Fig. 4.8. In Fig. 4.8, two droplets move towards the directions of Voronoi vectors and fill in the void space and two droplets move towards the opposite direction. This rearrangement event is a typical T1 neighbor-exchanging event. T1 event is a simplest topological rearrangement when a group of four droplets exchanges neighbors [81, 82]. When a T1 event happens, two droplets

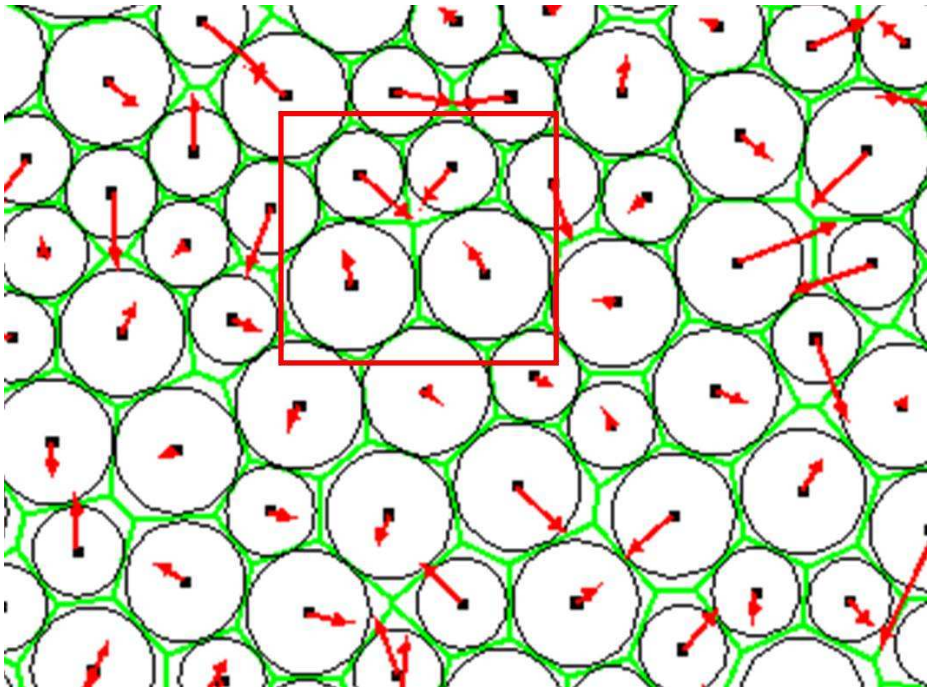

Figure 4.5: The Voronoi vector field with radical Voronoi cell and Delaunay triangulation. The Voronoi vectors are denoted by the red arrows. The region within the red square window is an example of an underpacked region.

move inward and two droplets move outward, which correspond to the two peaks of the histogram in Fig. 4.7. In conclusion, the Voronoi vectors are correlated with the droplets displacement directions and the feature of this correlation corresponds to the T1 rearrangement event during the slowly compressed process. Voronoi vector field is a good geometric analysis method that correlates geometric features and local dynamics in a jamming system.

As is mentioned in Section 4.3, the local divergence of the Voronoi vector field calculated over each Delaunay triangulation indicates the geometric features of the system. In Fig. 4.9 heavy red crosses represents negative local divergence in underpacked regions and light red crosses represents positive local divergence in overpacked

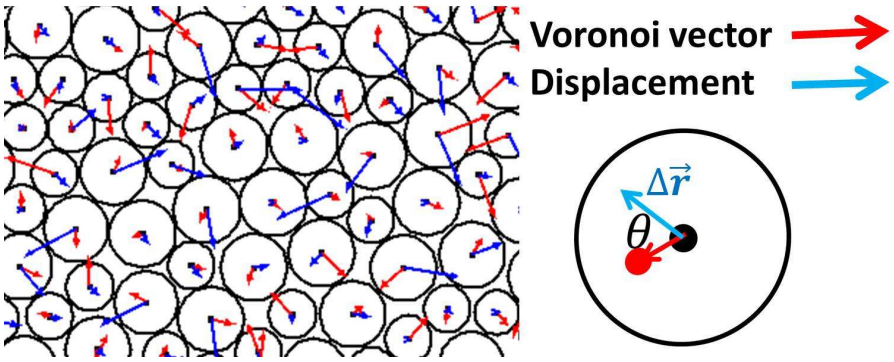

Figure 4.6: The red arrows indicate the direction of Voronoi vectors. The blue arrows show the direction of displacement for each droplet. The time interval for the displacement is 30s. θ is the angle between the direction of Voronoi vector and the direction of displacement of a certain droplet.

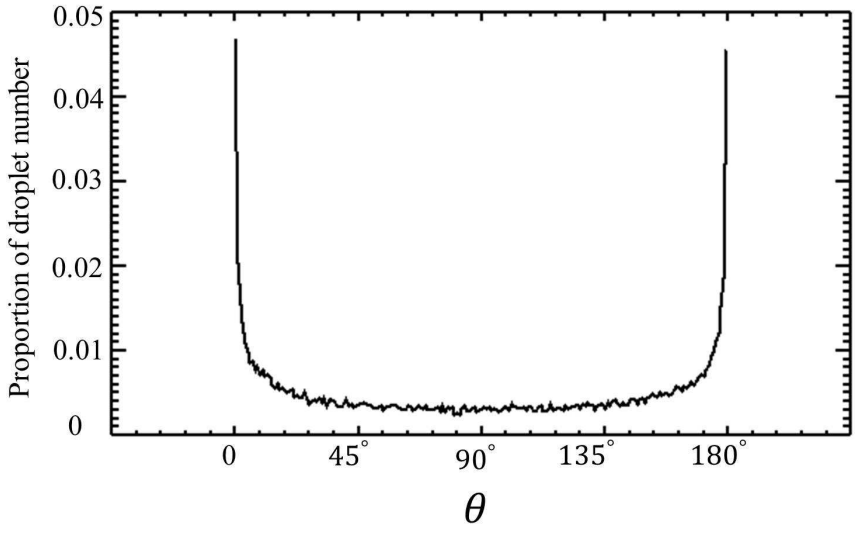

Figure 4.7: The histogram of θ. Y-axis is the proportion of the droplets in each bin. The curve peaks at 0° and 180° , which correspond to the droplets moving towards the Voronoi vector direction or go to the opposite direction.

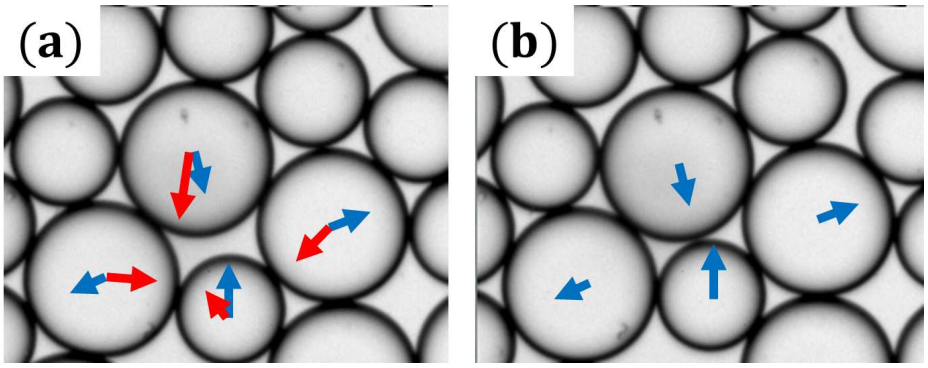

Figure 4.8: One example of T1 rearrangement. (a) The particle packing in experiment with red arrows demonstrating the Voronoi vectors and blue arrows showing the displacement of each droplets during the next $30s$.(b) The picture of particle packing in experiment with $\delta t = 30s$ after (a). The blue arrows showing the displacement of each droplets during the past $30s$, which are the same as the blue arrows in (a). In this process, two droplets move inward and two move outward.

regions. The red crosses in Fig. 4.10 demonstrate the local divergence for each Delaynay triangulation. Figure 4.11 (a) and (b) are two examples showing the correlation between the distribution of local divergence and the direction of droplet's motion. Figure 4.11 (a) is an example showing that the droplet moves towards the void space with lowest local divergence. And Fig. 4.11 (b) shows a droplet moving away from the void space with lowest local divergence. As is shown in Fig. 4.12, we define the angle, α, as the angle between the direction of displacement and the direction pointing towards the lowest local divergence. The histogram of the angle between the direction of the void space with lowest local divergence and the direction of displacement, Fig. 4.13, peaks at $0°$ and $180°$, which correspond to the two examples in Fig. 4.11.

We notice that there are two peaks in Fig. 4.7 and Fig. 4.13 which corresponds to the T1 neighbor-exchanging rearrangement event. Our question is: can we predict which peak the droplets are more likely to goes with, $0°$ or $180°$? In other word, in T1

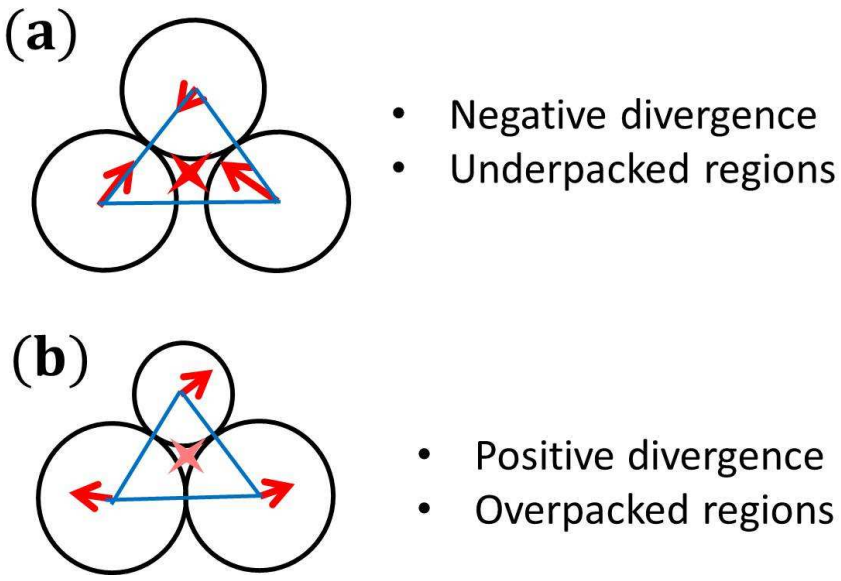

Figure 4.9: (a) This is an example of a Delaunay triangulation in a underpacked region. The three vertices of the triangulation correspond to the centers of three droplets. The void space among the three droplets is relatively large and the Voronoi vectors of the three droplets all point inward. Each Delaunay triangulaton corresponds to one local divergence. The local divergence of this Delaunay triangulation area is negative and we use a heavy cross to denote the negative local divergence. (b) This is an example of a Delaunay triangulation in an overpacked region. The Voronoi vectors of the three droplets point outward and the local divergence is positive. In this graph, we use a light cross to indicate an overpacked region with positive local divergence.

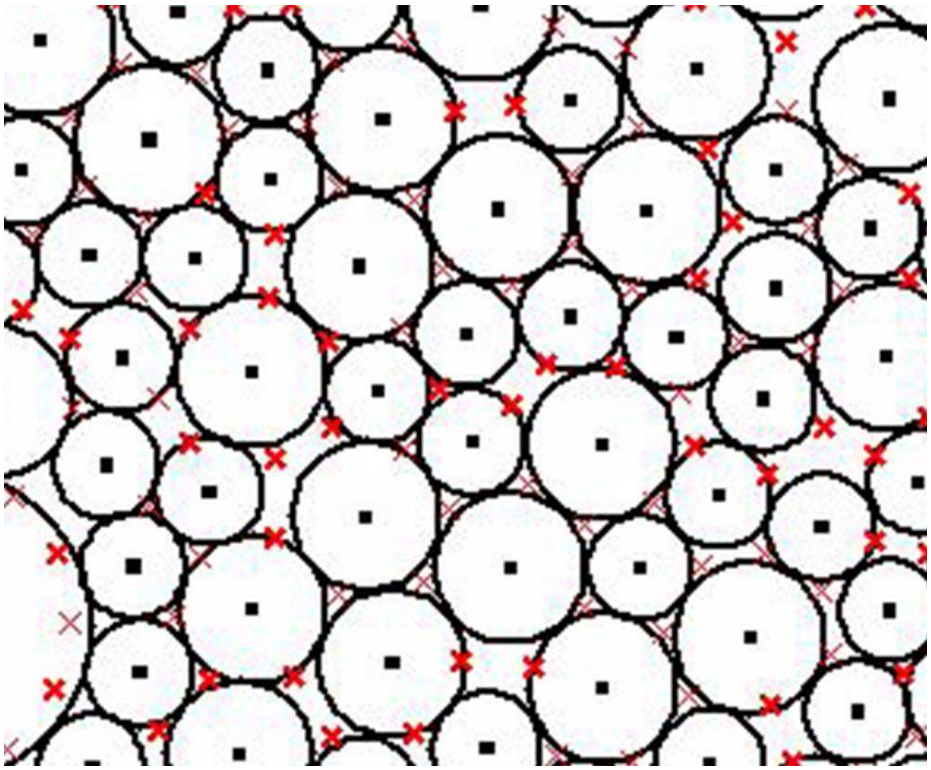

Figure 4.10: Droplet packing from experiment with red crosses indicates the sign of local divergence. Heavy crosses represent underpacked regions with negative local divergence and light crosses represent overpacked regions with positive local divergence.

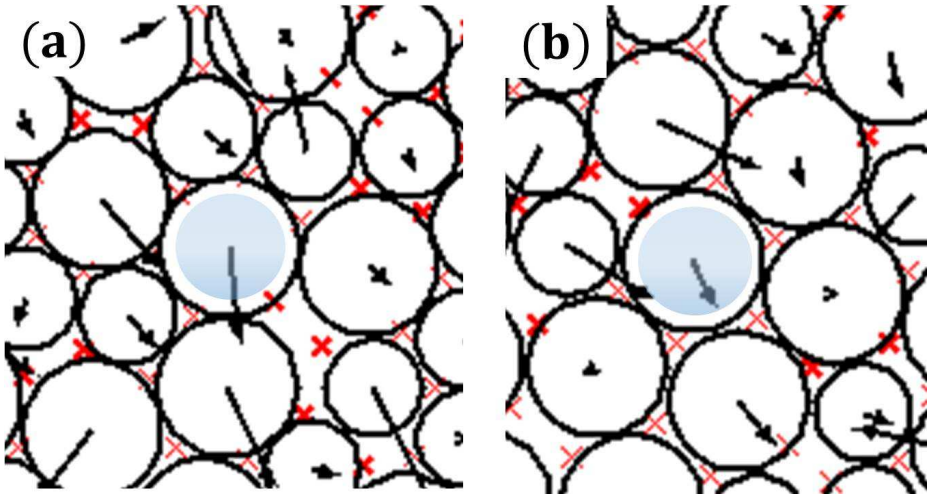

Figure 4.11: Droplet packing from experiment with red crosses indicates the sign of local divergence and black arrows show the direction of displacement. (a) Is an example showing that the droplet (blue) moves towards the direction of the lowest local divergence (underpacked region). (b) Is an example showing that the droplets (blue) moving away from the direction of the lowest local divergence.

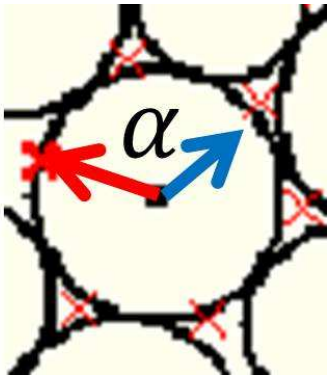

Figure 4.12: α is the angle between the direction of lowest local divergence (red) and the direction of displacement (black).

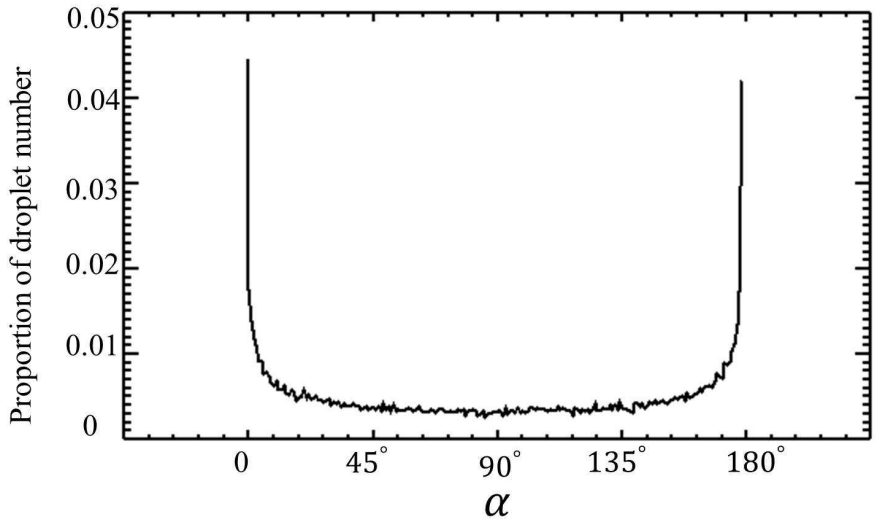

Figure 4.13: The histogram of α. Y-axis is the proportion of the droplets in each bin. The curve peaks at 0° and 180°, which correspond to the droplets moving towards the lowest local divergence direction or moving to the opposite direction.

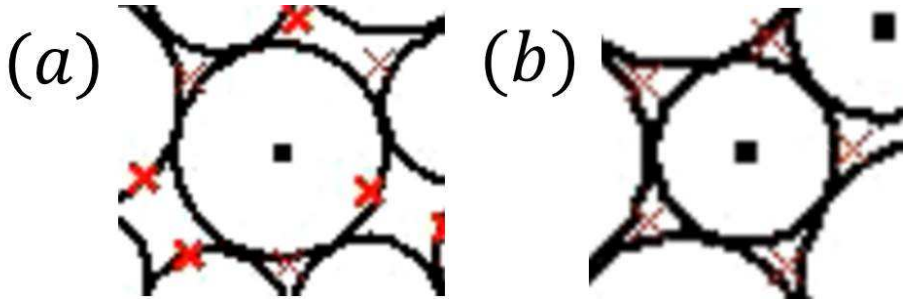

Figure 4.14: (a) An example of a droplet with large σ_D surrounded by heterogeneous structure. (b) An example of a droplet with small σ_D surrounded by homogeneous structure. The values of local divergence are denoted by red crosses: heavy cross represents small local divergence and light cross represents large local divergence.

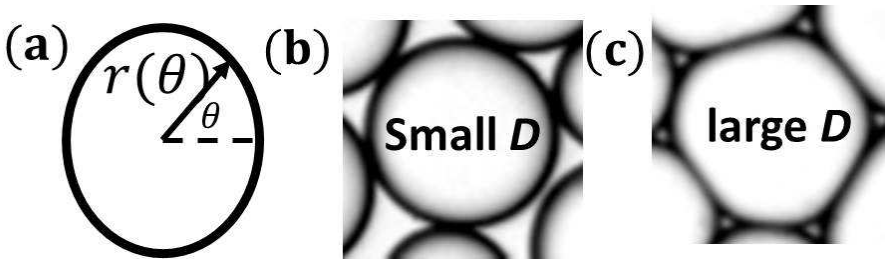

Figure 4.15: (a) A sketch of the outline of a deformed droplet. $r(\theta)$ is defined as the distance between the droplet mass center and the point on the outline for each point on the outline, where θ ranges from 0 to 2π. (b) An example droplet with small deformation, which is close to a perfect circle shape. $D = 0.015$ and $\phi = 0.89$. (c) An example droplet with large deformation. $D = 0.045$ and $\phi = 0.98$.

event, can we predict which two droplets move inward and which two droplets move outward based on the geometric and dynamic parameters of the system? To learn more about the directionality of the droplets motion, we define several geometric and dynamic parameters and study how they affect the droplets motion.

(1) Dynamics parameter, the magnitude of displacement. We use Δr to represent the magnitude of displacement of each droplet. Figure 4.16(a) shows the relation between $\cos\alpha$, where α is the angle between the displacement and the direction of lowest local divergence, with the dynamic parameter, the magnitude of displacement (Δr). It shows that the average value of $\cos\alpha$ with different Δr fluctuate around 0. The bin size in this graph is 0.1. So the magnitude of displacement does not influence the droplet's moving direction in a T1 event.

(2) Geometric parameter, standard deviation of divergence

The geometric environment surrounding a droplet is another potential factor in the directionality of a droplet's motion. As is shown in Fig. 4.4(c), each droplet is surrounded by several Delaunay triangulations and each triangle has a specific value

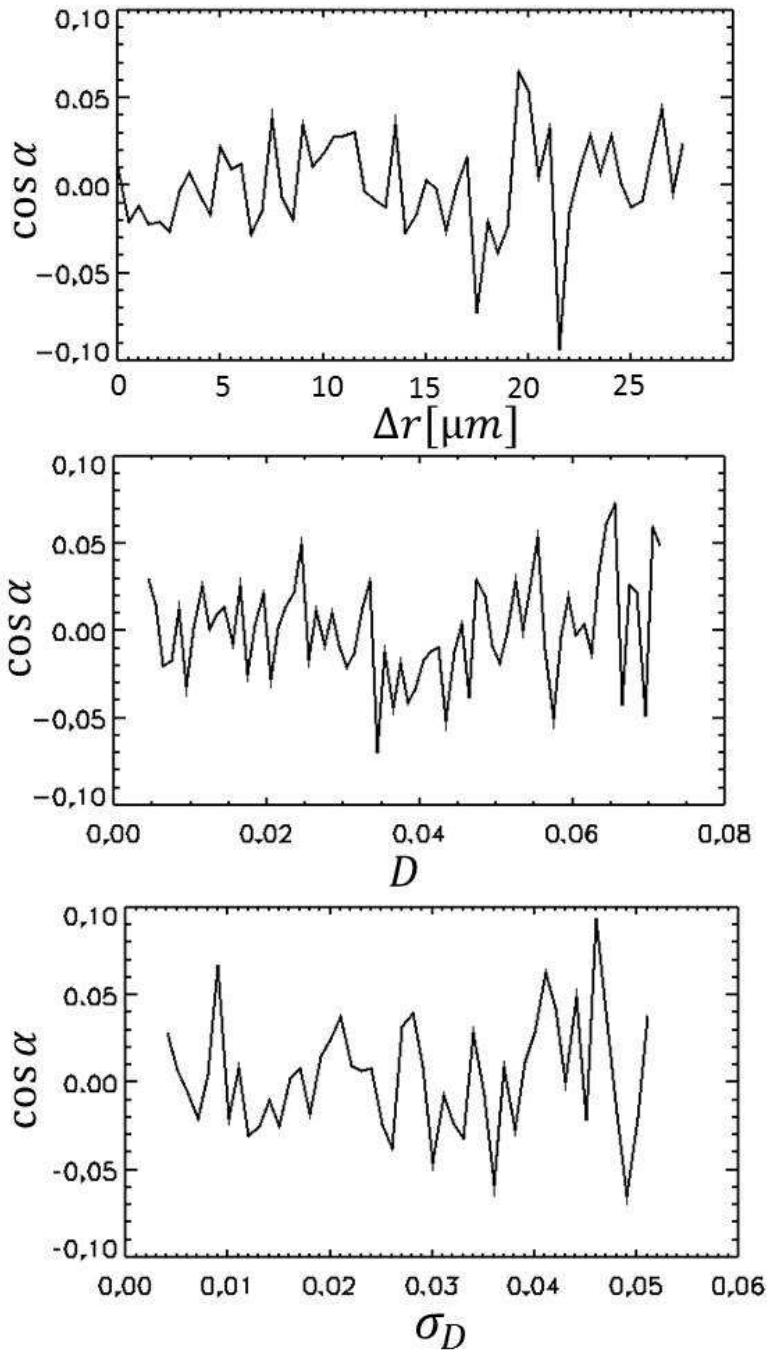

Figure 4.16: Average $\cos\alpha$ of droplets with different geometric and dynamic parameters, (a) Δr, (b) D and (c) σ_D. According to the symmetry of Fig. 4.13, average $\cos\alpha$ approximately equals to 0 which is consistent with the result in (a), (b) and (c). In T1 event, whether the droplets move inward the central void spaces or outward is independent of the parameters, (a) Δr, (b) D and (c) σ_D.

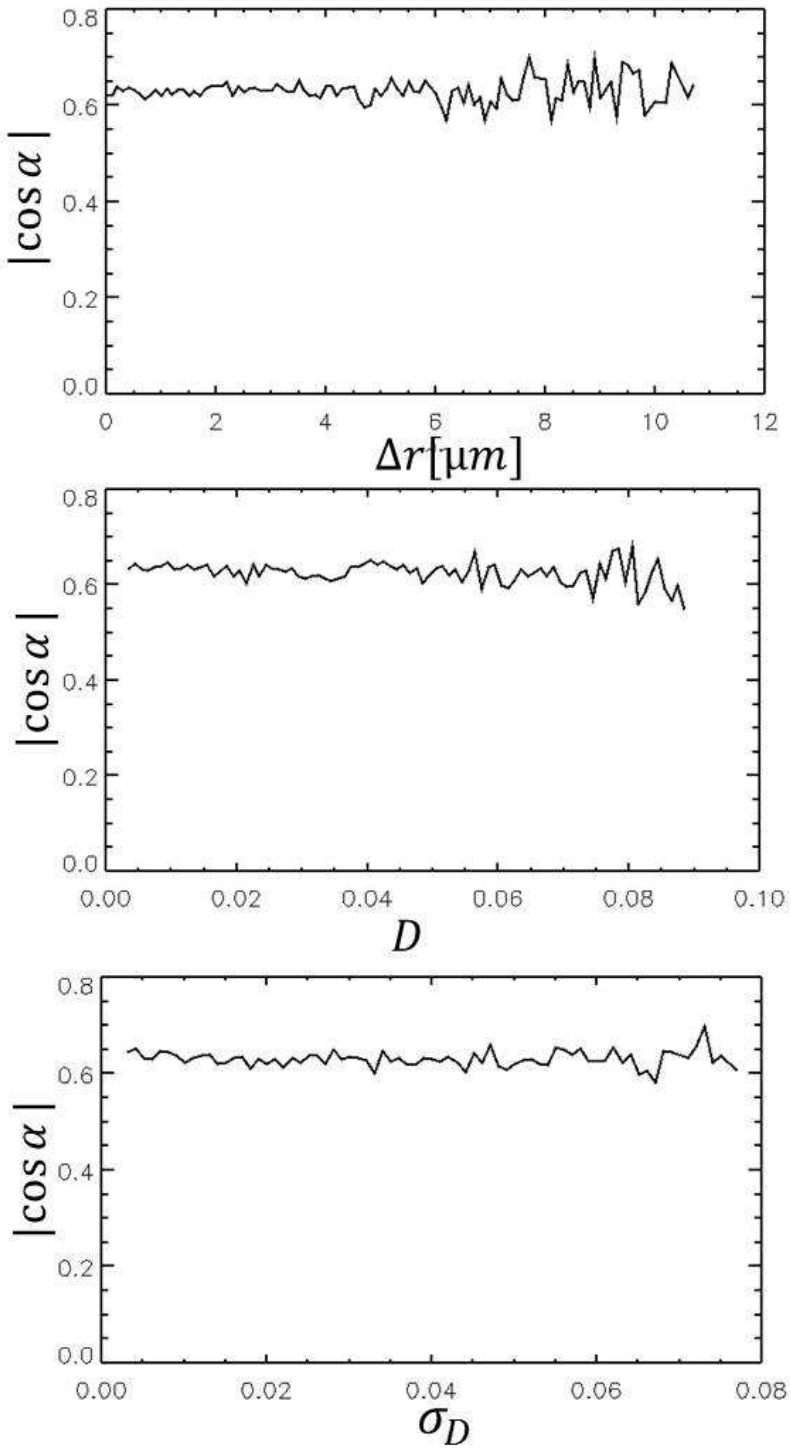

Figure 4.17: The dependence of $|\cos\alpha|$ on the parameters, (a) Δr, (b) D and (c) σ_D. The three curves in (a), (b) and (c) all slightly fluctuate around the mean value, $|\cos\alpha| \approx 0.63$.

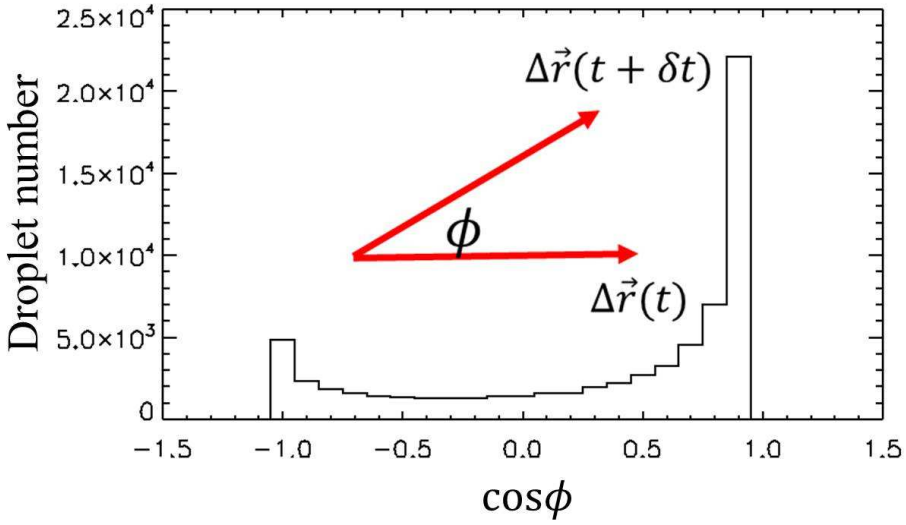

Figure 4.18: Histogram of $\cos\phi$ for all the droplets during the whole slowly compressed process. Inset shows the definition of ϕ, the angle between the displacement at t and the displacement at $t + \delta t$.

of its local divergence. To quantify the geometric features of a droplet, we define the standard deviation of the values of local divergence for each droplet as σ_D. Large σ_D indicates that the droplet is surrounded by heterogeneous local structure and small σ_D indicates homogeneous local structure. As is shown in Fig. 4.10, each droplet belongs to several Delaunay triangulation and each triangle has a corresponding local divergence. In Fig. 4.14(a), the droplet is surrounded by seven heterogenously distributed void space. In this case, the standard deviation of the local divergence for this droplet is relatively large. The droplet in Fig. 4.14 (b) is surrounded by homogenously distributed local divergence and the standard deviation is relatively small. Figure 4.16(b) shows the relation between $\cos\alpha$ and σ_D. The average value of $\cos\alpha$ with different σ_D fluctuate around 0. Thus, the directionality of droplet rearrangement doesn't depend on its geometric properties, σ_D.

(3) Shape of the droplet, deformation

As the system slowly jams, the droplets get close and exert stress on their neighbors and deform into irregular shapes. We define a parameter, deformation, D, to quantify the stress between droplets and their touching neighbors. As is shown in Fig. 4.4, we identify the outline of each droplet, measure the radius $r(\theta)$ at each point on the outline (the distance between the droplet mass center and the point on the outline), and define the droplet deformation as the standard deviation of $r(\theta)$ normalized by the droplet's mean radius [82],

$$D = \frac{\sigma_{r(\theta)}}{\langle r(\theta) \rangle}. \tag{4.4}$$

Figure 4.4 (b) is an example droplet with small deformation which is close to a circular shape and Fig. 4.4 (c) is an example of a droplet with large deformation. Both of the examples come from experimental data. Figure 4.16(c) shows the independence of the direction of motion, $\cos\alpha$, and the deformation of a droplet.

Figure 4.16 shows that the directionality of droplet rearrangement doesn't depend on Δr, D or σ_D. As a supplemental support for our conclusion, Fig. 4.17 checks if the bias of the directionality towards 0° or 180° is more pronounced with different Δr, D and σ_D values. In Fig. 4.17, the curves are relatively flat with small fluctuations around the average value, which demonstrates the independence of $|\cos\alpha|$ on Δr, D and σ_D.

According to the experimental result in Fig. 4.18, the directionality of droplets motion at time $t + \delta t$ is more likely decided by the direction of displacement at the previous time t. Figure 4.18 is the histogram of $\cos\phi$, where ϕ is the angle between the displacement at time t, $\Delta\vec{r}_t$. and the displacement at time $t + \delta t$, $\Delta\vec{r}_{t+\delta t}$. In this

experiment, $\delta t = 30s$. According to experimental result, ϕ peaks at $0°$, which means that the droplets are more likely to move towards the same direction as the direction of the previous displacement.

In this section, we figure out the correlation between the droplet's motion direction and the Voronoi vector field. Furthermore, we find the correlation between T1 rearrangement events and the Voronoi vector field in this slowly compressed system. In T1 rearrangement event, the directionality of displacement is independent of deformation, the standard deviation of local divergence and the magnitude of displacement. It is related to the previous motion of a certain droplet and behaves like an 'inertial effect'. However, rather than inertia, we believe that the true reason for this behavior is due to the overdamping of the slowly compressed system.

4.5 The Magnitude of Droplet Displacement

As is demonstrated in Sec.4.3, the Voronoi vector indicates the geometric structure surrounding a certain droplet. The droplets surrounded by unevenly distributed large void space have large Voronoi vectors. We anticipate that there is a correlation between the local geometric structure and the dynamics of the droplet. Figure 4.19 shows the relation between the length of Voronoi vector and the magnitude of displacement of each droplet. The x-axis is the droplet displacement in μm and y-axis is the average Voronoi vector length of the droplets with the specific displacement. The average value is calculated for the droplets throughout the whole compressing process. According to Fig. 4.19, the droplets with larger Δr have longer Voronoi vectors. The graph relates the magnitude of droplets displacement with the Voronoi

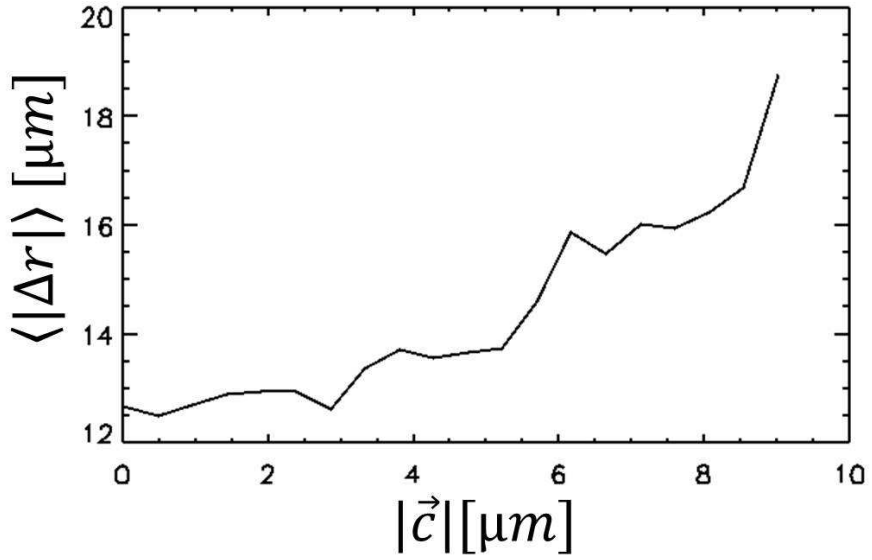

Figure 4.19: The positive correlation between the magnitude of displacement and the length of Voronoi vector. Each point on the curve corresponds to the average displacement magnitude of the droplets with a certain range of modulus of Voronoi vectors.

vectors. Voronoi vector field is a good geometric analysis characterizing the dynamics of the slow jamming emulsion system.

To study the relation between the local divergence of Voronoi vector field, we introduce a parameter, σ_D the standard deviation of local divergence for each droplets. In Fig. 4.14, the droplets are surrounded by several voids and each void has its local divergence. In Fig. 4.14 (a), the droplet is surrounded by seven heterogeneously distributed voids. In this case, the standard deviation of the local divergence for this droplet is relatively large. The droplet in Fig. 4.14 (b) is surrounded by homogeneously distributed local divergence and the standard deviation is relatively small. Figure 4.20 shows that droplets with large σ_D exhibit larger displacement. In other

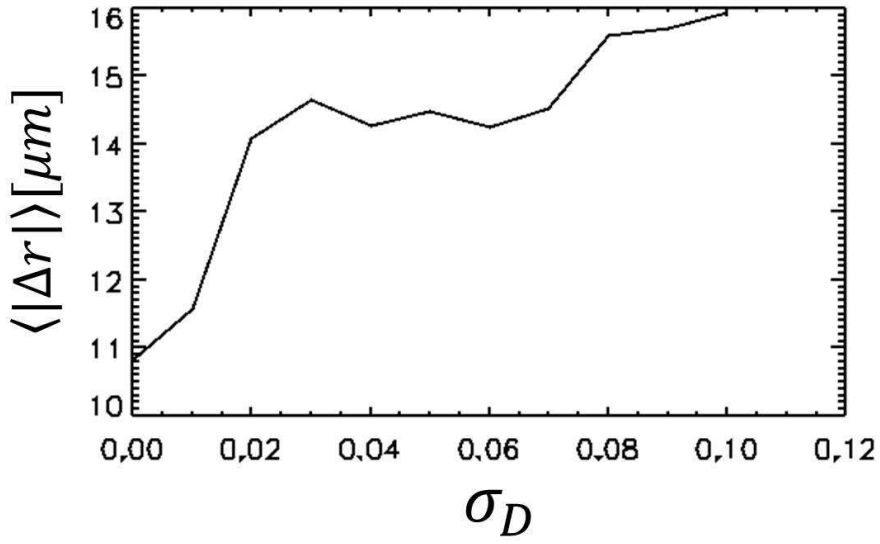

Figure 4.20: The positive correlation between the magnitude of displacement and σ_D.

word, the droplets surrounded by heterogeneous neighbour structure are more likely to rearrange.

In this section, we study the magnitude of droplet dynamics and find a positive correlation between Δr and Voronoi vector field. With longer Voronoi vectors, the droplets occupy less space in its Voronoi cell and leave larger void space, so they are more likely to rearrange. In addition, with larger σ_D, the droplets locate in heterogenous environment and they are more likely to exhibit local neighbor-changing event.

4.6 Evolution of Geometric and Dynamic Parameters in Jamming Systems

As is mentioned in Sec.4.2, as water slowly evaporates from the opening side of the chamber, the system gets more crowded and the droplets fill in the void space and exert stress on their neighbor droplets. In this section, we explore how the dynamic and geometric parameters of the system evolve during this slowly compressed progress.

Figure 4.21 presents a big picture for the dynamic and structural evolution in the slowly compressed system. (1) The standard deviation of local divergence , σ_D, decreases as area fraction increases. This result is consistent with the result published in Rieser's paper [1]. (2) Droplet motion slows down during this compressed process. And this slowing down is more obviously at higher area fraction stage, which is consistent with our observation that much fewer rearrangement events occur in the end of the evaporation process. (3) The stress between neighbor droplets, quantified by deformation, increases as area fraction increases due to insufficient free space.

Furthermore, Fig. 4.21 implies some correlation between the three parameters, σ_D, Δr and D. Figure 4.20 shows that the droplet displacement is faster with high σ_D, which is consist with Fig. 4.21. Figure 4.22 shows that deformation decreases as σ_D increases, indicating that the droplets in homogeneous structure are more deformed. This phenomenon is obvious at the high area fraction stage when droplets experience homogeneously distributed stress from their neighbors. Figure 4.23 shows the correlation between displacement and deformation. The droplets with small deformation are more likely to exhibit large displacement, or rearrange. On the other hand, with

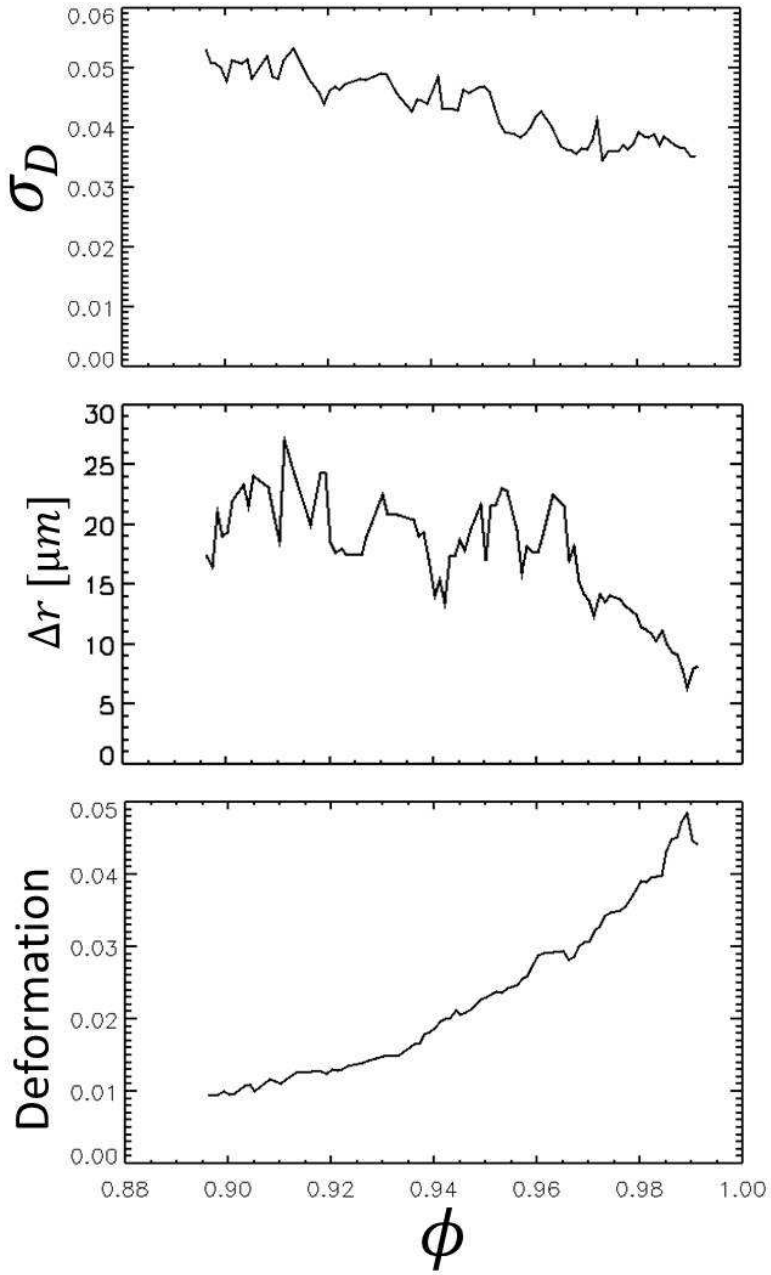

Figure 4.21: (a) σ_D decreases as the area fraction increases, which means that the structure of the system become homogeneous during the slowly jamming process. (b) The droplet dynamics, represented by the magnitude of droplet displacement, slows down as the area fraction increases. (c) Deformation, D, increases as area fraction increases.

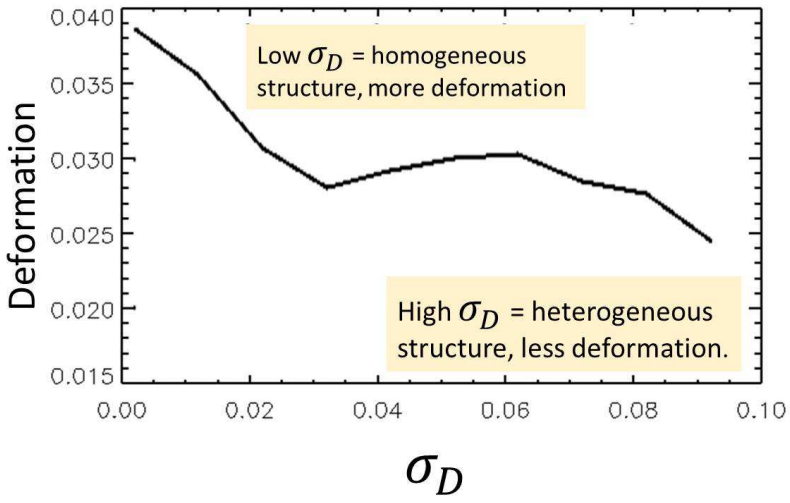

Figure 4.22: The relationship between deformation and σ_D. Each dot on the curve represents the average deformation of the droplets with σ_D value in a certain small range. The droplets with high σ_D are surrounded by homogeneous structure and they are more deformed. The droplets with low σ_D are surrounded by heterogeneous structure and they are less deformed.

large deformation, a droplet is caged by its neighbors and hard to escape. As a summary of Fig. 4.20, 4.22 and 4.23, Fig. 4.24 is a diagram showing the correlations of the parameters: when area fraction increases, displacement slows down,deformation increases, and σ_D decreases. In addition, area fraction might also affect the relation between the three parameters, σ_D, Δr and D.

Is the correlation between Δr and D, as is shown in Fig. 4.23 due to the changing of area fraction? To answer this question, we studied the dependence of displacement fluctuation on deformation. The displacement fluctuation Δr_{fluc} is defined as the displacement normalized by the average displacement at each time, $\Delta r_{fluc} = \frac{\Delta r}{<\Delta r>_t}$. Figure 4.25 doesn't shown any correlation between Δr_{fluc} and deformation. The decreasing of Δr is mostly due to the increase of area fraction. In other word, in

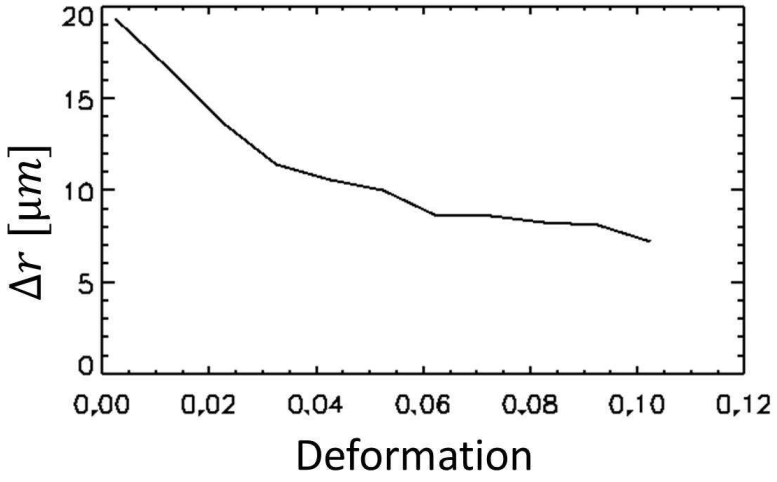

Figure 4.23: The relationship between Δr with $\Delta t = 30s$ and deformation. Each dot on the curve represents the average Δr of the droplets with deformation in a certain small range. The droplets that less deformed are more likely to exhibit large displacement.

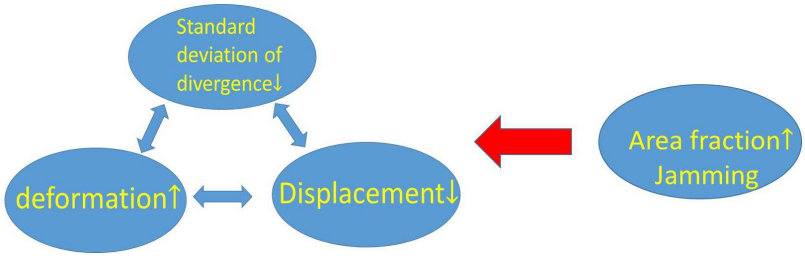

Figure 4.24: Diagram demonstrates the correlations between area fraction, standard deviation of local divergence, magnitude of displacement and deformation.

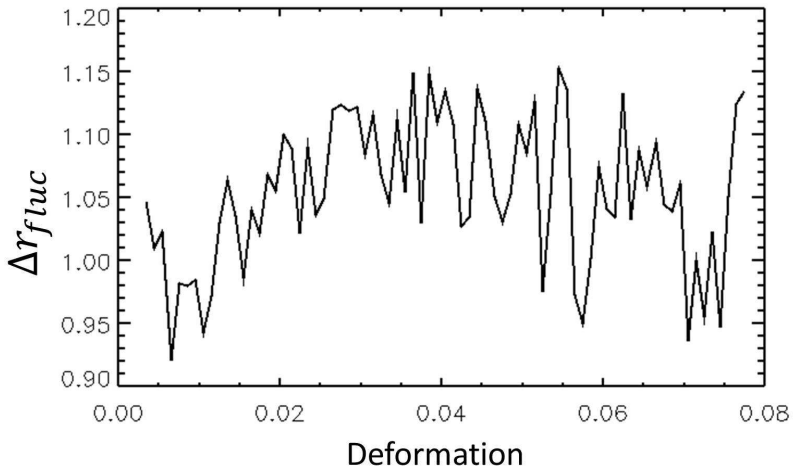

Figure 4.25: The fluctuation of droplet displacement is independent of the deformation of each droplet.

a system with a certain area fraction, the droplets with large deformation are not necessarily moving slower or more stable.

4.7 Conclusion

We studied the cooperative rearrangements of a slowly compressed 2-D emulsion system. By characterizing the local structural heterogeneity based on the Voronoi Vector field [1], we find the correlation between the cooperative rearrangement and the local structural heterogeneity. The droplets which locate in a heterogeneous environment are more likely to exhibit cooperative rearrangement. In the corresponding cooperative rearrangement, two droplets move away from the void space and two droplets move inwards the void space, which is known as T1 event. The directionality of the droplets' motion in T1 events is not influenced by the droplet's deformation

or the geometric features of the surrounding environment. In other words, we cannot distinguish which two droplets move inward and which two move outward in T1 events according to the local structural heterogeneity of the system. The evolution of geometric and dynamic parameters as jamming are also one interesting aspect in this research due to the long-time-scaled compressing process. During this slowly jamming process, the area fraction of the system slowly increases. The standard deviation of local divergence decreases which is consistent with the result published by Rieser [1]. The droplets motion slows down and fewer rearrangement events occur. The deformation of droplets increases due to the insufficiency of free space. And the negative correlation between the displacement of droplets and deformation is due to the increase of area fraction. This experimental research reveals the strong correlation between the structural heterogeneity and the local rearrangement in a slowly compressed emulsion system.

4.8 Discussion

Since a T1 event involves four adjacent droplets, characterizing the structural heterogeneity of the four adjacent droplets is potentially a better way to relating the structural properties of the system with the rearrangement during the jamming process. The local divergence D_k, defined in Chap. 4.3, is based on the three Voronoi vectors in a Delaunay triangle. Since a T1 event involves four adjacent droplets, considering the local divergence of the four corresponding Voronoi vectors of the four adjacent droplets could be a better way to characterize the structural properties. And since the collection of four adjacent droplets involves two Delaunay triangles, we

could learn more structural features for T1 events by considering the divergences of the two Delaunay triangles as a pair and comparing their values. In this way, we can make the connection between the structural properties with T1 event and potentially be able to accurately predict which four droplets are going to exhibit a T1 event according to their structural properties.

Chapter 5

Summary

Soft materials have a variety of applications in industry due to their interesting mechanical response in the transition between a solid-like state and a liquid-like state. In 1998, Liu and Nagel proposed that disordered materials all experience a universal process, a jamming transition, when they transit from a liquid-like state to a solid-like state [4]. The key idea of jamming transition is that the transitions to rigid state in disordered materials are due to a universal underlying physics [5]. To understand the universal underlying physics of jamming transition, we study the mechanics, geometry, time scaling and the energy landscape of jamming systems. By building up the correlation between cooperative dynamics, the geometrical properties and the free energy landscapes of jamming systems, we (hopefully) reveal more clues for the universality of jamming transition than previous research.

In Chap. 2, we study glassy dynamics using a simulation of three soft Brownian particles confined to a two-dimensional circular region. If the circular region is large, the disks freely rearrange, but rearrangements are rarer for smaller system sizes. We

directly measure a one-dimensional free energy landscape characterizing the dynamics. This landscape has two local minima corresponding to the two distinct disk configurations, separated by a free energy barrier which governs the rearrangement time scale. With a higher free energy barrier, the time scale for cooperative rearrangement is longer. We study several different interaction potentials, including finite range potentials (harmonic potential and WCA potential) and infinite range potentials (Lennard-Jones potential and long-range potential), and demonstrate that the free energy barrier is composed of a potential energy barrier and an entropic barrier. This simple model provides us a complete and clear view of free energy landscape and demonstrates the connections between the free energy landscape, free energy barriers, and non-Arrhenius temperature dependence. For fixed system size R, the potential energy landscape is independent of T, yet the effective potential energy barrier height, entropic barrier height, and overall free energy barrier all depend on T. This leads to non-Arrhenius temperature dependence. The data computed with forward flux sampling for harmonic potential model, shows that the transition time scale has an Arrhenius temperature dependent component, $U_{\min}$, where T-independent $U_{\min}$ is the minimum potential energy barrier when the particles transit with an optimized path. The data of forward flux sampling also verify our theoretical conjecture that the non-Arrenius component of the free energy barrier follows the relation with temperature as $\beta F \sim |\ln T|$ when $T \to 0$.

For the cases with more particles, we anticipate that entropy plays an even more important role in cooperative rearrangements, as suggested in 1965 by Adam and Gibbs [25] and discussed by many authors subsequently. In our model, the transition

across the free energy barrier requires cooperative motion of all three particles which results in an entropic penalty, which is consistent with the spirit of Adam and Gibbs.

In Chap. 3, we introduce a method to map the particles with soft interaction potentials onto hard particles with some effective size by treating the particles in a pair-wise fashion. And this method works for the finite-range potentials (harmonic and WCA) and only for original system sizes $R > 3$(HM) and $R > 3.24$(WCA). It does not work for system with small confinement due to the high entropy compensate to reach the theoretic minimum potential energy, $U_{\min}$. By building up the connection between soft/deformable and hard particles using this method, we can better understand the influence of interaction potentials in jamming transition.

In Chap. 4, we study the correlation between the cooperative rearrangement and the local structural heterogeneity in a slowly compressed quasi-2D emulsion system. We qualify the local structural heterogeneity based on the Voronoi vector field [1]. Our experimental result shows that the droplets which locate in a heterogeneous environment are more likely to exhibit cooperative rearrangement. In the corresponding cooperative rearrangement, two droplets move away from the void space and two droplets move inward the void space, which is known as T1 event. The directionality of the droplets' motion in T1 events is not influenced by the droplet's deformation or the geometric features of the surrounding environment. In other words, we cannot distinguish which two droplets move inward and which two move outward in T1 events according to the local structural heterogeneity of the system. The evolution of geometric and dynamic parameters as jamming is also one interesting aspect in this research due to the long-time-scaled compressing process. During this slowly

jamming process, the area fraction of the system slowly increases. The standard deviation of local divergence decreases which is consistent with the result published by Rieser [1]. The droplets motion slows down and fewer rearrangement events occur. The deformation of droplets increases due to the insufficiency of free space. And the negative correlation between the displacement of droplets and deformation is due to the increase of area fraction. This experimental research reveals the strong correlation between the structural heterogeneity and the local rearrangement in a slowly compressed emulsion system.

Bibliography

[1] J. M. Rieser, C. P. Goodrich, A. J. Liu, and D. J. Durian, Divergence of Voronoi Cell Anisotropy Vector: A Threshold-Free Characterization of Local Structure in Amorphous Materials, *Phys. Rev. Lett.*, **116**, 088001 (2016).

[2] M. V. Hecke, Jamming of soft particles: geometry, mechanics, scaling and isostaticity, *Journal of Physics: Condensed Matter*, **22**, 033101 (2010).

[3] R. A. L. Jones, *Soft Condensed Matter (Oxford Master Series in Condensed Matter Physics, Vol. 6)* (Oxford University Press), 1st edition (2002), ISBN 0198505892.

[4] A. J. Liu and S. R. Nagel, Nonlinear dynamics: Jamming is not just cool any more, *Nature*, **396**, 21–22 (1998).

[5] G. Biroli, Jamming: A new kind of phase transition?, *Nat Phys*, **3**, 222–223 (2007).

[6] V. Trappe, V. Prasad, L. Cipelletti, P. N. Segre, and D. A. Weitz, Jamming phase diagram for attractive particles, *Nature*, **411**, 772–775 (2001).

[7] C. S. O'Hern, L. E. Silbert, A. J. Liu, and S. R. Nagel, Reply to 'Comment on

"Jamming at zero temperature and zero applied stress: The epitome of disorder" ', *Phys. Rev. E*, **70**, 043302 (2004).

[8] A. J. Liu and S. R. Nagel, The jamming transition and the marginally jammed solid, *Ann. Rev. Cond. Mat. Phys.*, **1**, 347–369 (2010).

[9] N. Xu, T. K. Haxton, A. J. Liu, and S. R. Nagel, Equivalence of glass transition and colloidal glass transition in the hard-sphere limit, *Phys. Rev. Lett.*, **103**, 245701 (2009).

[10] W. van Megen and P. N. Pusey, Dynamic light-scattering study of the glass transition in a colloidal suspension, *Physical Review A*, **43**, 5429–5441 (1991).

[11] T. G. Mason and D. A. Weitz, Linear Viscoelasticity of Colloidal Hard Sphere Suspensions near the Glass Transition, *Physical Review Letters*, **75**, 2770–2773 (1995).

[12] W. van Megen, T. C. Mortensen, S. R. Williams, and J. Müller, Measurement of the self-intermediate scattering function of suspensions of hard spherical particles near the glass transition, *Physical Review E*, **58**, 6073–6085 (1998).

[13] W. van Megen and S. R. Williams, Comment on "probing the equilibrium dynamics of colloidal hard spheres above the Mode-Coupling glass transition", *Phys. Rev. Lett.*, **104**, 169601 (2010).

[14] F. Bolton and D. Weaire, Rigidity loss transition in a disordered 2D froth, *Physical Review Letters*, **65**, 3449–3451 (1990).

[15] F. H. Stillinger, A Topographic View of Supercooled Liquids and Glass Formation, *Science*, **267**, 1935–1939 (1995).

[16] M. Mézard and G. Parisi, A first-principle computation of the thermodynamics of glasses, *The Journal of Chemical Physics*, **111**, 1076–1095 (1999).

[17] D. Wales, *Energy Landscapes* (Energy Landscapes, by David Wales, pp.˜692.˜ISBN 0521814154.˜Cambridge, UK: Cambridge University Press, March 2004.) (2004).

[18] F. Colomo and A. G. Pronko, Square ice, alternating sign matrices, and classical orthogonal polynomials, *J. Stat. Mech. Theory Exp.* (2005).

[19] M. Goldstein, Viscous liquids and the glass transition: A potential energy barrier picture, *J. Chem. Phys.*, **51**, 3728–3739 (1969).

[20] P. G. Debenedetti and F. H. Stillinger, Supercooled liquids and the glass transition, *Nature*, **410**, 259–267 (2001).

[21] A. Heuer, Exploring the potential energy landscape of glass-forming systems: from inherent structures via metabasins to macroscopic transport, *J. Phys.: Cond. Matter*, **20**, 373101 (2008).

[22] F. H. Stillinger and T. A. Weber, Hidden structure in liquids, *Physical Review A*, **25**, 978–989 (1982).

[23] D. C. Wallace, Statistical mechanics of monatomic liquids, *Phys. Rev. E*, **56**, 4179–4186 (1997).

[24] T. Yoshidome, A. Yoshimori, and T. Odagaki, Free energy landscape and cooperatively rearranging region in a hard sphere glass, *Physical Review E*, **76**, 021506+ (2007).

[25] G. Adam and J. H. Gibbs, On the temperature dependence of cooperative relaxation properties in glass-forming liquids, *J. Chem. Phys.*, **43**, 139–146 (1965).

[26] R. K. Bowles and R. J. Speedy, Five discs in a box, *Physica A*, **262**, 76–87 (1999).

[27] P. R. Wolde and D. Frenkel, Enhancement of Protein Crystal Nucleation by Critical Density Fluctuations, *Science*, **277**, 1975–1978 (1997).

[28] A. Heuer, Information content of multitime correlation functions for the interpretation of structural relaxation in glass-forming systems, *Physical Review E*, **56**, 730+ (1997).

[29] S. V. Krivov and M. Karplus, Hidden complexity of free energy surfaces for peptide (protein) folding., *Proc Natl Acad Sci U S A*, **101**, 14766–14770 (2004).

[30] A. Altis, M. Otten, P. H. Nguyen, R. Hegger, and G. Stock, Construction of the free energy landscape of biomolecules via dihedral angle principal component analysis, *The Journal of Chemical Physics*, **128**, 245102+ (2008).

[31] G. Maisuradze, A. Liwo, and H. Scheraga, Principal Component Analysis for Protein Folding Dynamics, *Journal of Molecular Biology*, **385**, 312–329 (2009).

[32] G. Biroli and J. P. Garrahan, Perspective: The glass transition, *J. Chem. Phys.*, **138**, 12A301 (2013).

[33] M. D. Ediger and P. Harrowell, Perspective: Supercooled liquids and glasses, *J. Chem. Phys.*, **137**, 080901 (2012).

[34] A. Cavagna, Supercooled liquids for pedestrians, *Phys. Rep.*, **476**, 51–124 (2009).

[35] J. C. Dyre, *Colloquium* : The glass transition and elastic models of glass-forming liquids, *Rev. Mod. Phys.*, **78**, 953–972 (2006).

[36] C. A. Angell, K. L. Ngai, G. B. McKenna, P. F. McMillan, and S. W. Martin, Relaxation in glassforming liquids and amorphous solids, *J. App. Phys.*, **88**, 3113–3157 (2000).

[37] L. Cipelletti and L. Ramos, Slow dynamics in glasses, gels and foams, *Curr. Op. Coll. Int. Sci.*, **7**, 228–234 (2002).

[38] P. G. Debenedetti and F. H. Stillinger, Supercooled liquids and the glass transition, *Nature*, **410**, 259–267 (2001).

[39] F. H. Stillinger, A topographic view of supercooled liquids and glass formation, *Science*, **267**, 1935–1939 (1995).

[40] F. Sciortino, Potential energy landscape description of supercooled liquids and glasses, *J. Stat. Mech.*, **2005**, P05015 (2005).

[41] F. H. Stillinger and T. A. Weber, Hidden structure in liquids, *Physical Review A*, **25**, 978–989 (1982).

[42] S. Sastry, P. G. Debenedetti, and F. H. Stillinger, Signatures of distinct dynamical regimes in the energy landscape of a glass-forming liquid, *Nature*, **393**, 554–557 (1998).

[43] T. Pérez-Castañeda, R. J. Jiménez-Riobóo, and M. A. Ramos, Two-level systems and boson peak remain stable in 110-million-year-old amber glass, *Phys. Rev. Lett.*, **112**, 165901 (2014).

[44] P. Charbonneau, J. Kurchan, G. Parisi, P. Urbani, and F. Zamponi, Fractal free energy landscapes in structural glasses, *Nature Comm.*, **5**, 3725 (2014).

[45] F. H. Stillinger and T. A. Weber, Packing structures and transitions in liquids and solids, *Science*, **225**, 983–989 (1984).

[46] M. H. Cohen and D. Turnbull, Molecular transport in liquids and glasses, *J. Chem. Phys.*, **31**, 1164–1169 (1959).

[47] L. V. Woodcock and C. A. Angell, Diffusivity of the hard-sphere model in the region of fluid metastability, *Phys. Rev. Lett.*, **47**, 1129–1132 (1981).

[48] R. J. Speedy, The hard sphere glass transition, *Mol. Phys.*, **95**, 169–178 (1998).

[49] R. K. Bowles and R. J. Speedy, Five discs in a box, *Physica A*, **262**, 76–87 (1999).

[50] S. S. Ashwin and R. K. Bowles, Complete jamming landscape of confined hard discs, *Phys. Rev. Lett.*, **102**, 235701 (2009).

[51] G. L. Hunter and E. R. Weeks, Free-energy landscape for cage breaking of three hard disks, *Phys. Rev. E*, **85**, 031504 (2012).

[52] D. N. Perera and P. Harrowell, Relaxation dynamics and their spatial distribution in a two-dimensional glass-forming mixture, *J. Chem. Phys.*, **111**, 5441–5454 (1999).

[53] B. Doliwa and A. Heuer, Cooperativity and spatial correlations near the glass transition: Computer simulation results for hard spheres and disks, *Phys. Rev. E*, **61**, 6898–6908 (2000).

[54] L. Berthier and T. A. Witten, Glass transition of dense fluids of hard and compressible spheres, *Phys. Rev. E*, **80**, 021502 (2009).

[55] M. Schmiedeberg, T. K. Haxton, S. R. Nagel, and A. J. Liu, Mapping the glassy dynamics of soft spheres onto hard-sphere behavior, *Europhys. Lett.*, **96**, 36010 (2011).

[56] C. A. Angell, Formation of glasses from liquids and biopolymers, *Science*, **267**, 1924–1935 (1995).

[57] D. J. Durian, Foam mechanics at the bubble scale, *Phys. Rev. Lett.*, **75**, 4780–4783 (1995).

[58] C. S. O'Hern, L. E. Silbert, A. J. Liu, and S. R. Nagel, Jamming at zero temperature and zero applied stress: The epitome of disorder, *Phys. Rev. E*, **68**, 011306 (2003).

[59] J. E. Lennard-Jones, Cohesion, *Proc. Phys. Soc.*, **43**, 461–482 (2002).

[60] H. C. Andersen, J. D. Weeks, and D. Chandler, Relationship between the hard-sphere fluid and fluids with realistic repulsive forces, *Phys. Rev. A*, **4**, 1597–1607 (1971).

[61] N. Metropolis, A. W. Rosenbluth, M. N. Rosenbluth, A. H. Teller, and E. Teller,

Equation of state calculations by fast computing machines, *J. Chem. Phys.*, **21**, 1087–1092 (1953).

[62] C. P. Royall, W. C. K. Poon, and E. R. Weeks, In search of colloidal hard spheres, *Soft Matter*, **9**, 17–27 (2013).

[63] C. Vogler, F. Bruckner, B. Bergmair, T. Huber, D. Suess, and C. Dellago, Simulating rare switching events of magnetic nanostructures with forward flux sampling, *Phys. Rev. B*, **88**, 134409 (2013).

[64] D. Moroni, T. S. van Erp, and P. G. Bolhuis, Simultaneous computation of free energies and kinetics of rare events, *Physical Review E (Statistical, Nonlinear, and Soft Matter Physics)*, **71** (2005).

[65] F. A. Escobedo, E. E. Borrero, and J. C. Araque, Transition path sampling and forward flux sampling. Applications to biological systems, *Journal of Physics: Condensed Matter*, **21**, 333101+ (2009).

[66] R. J. Allen, P. B. Warren, and P. R. ten Wolde, Sampling Rare Switching Events in Biochemical Networks, *Physical Review Letters*, **94**, 018104+ (2005).

[67] K. Kratzer, A. Arnold, and R. J. Allen, Automatic, optimized interface placement in forward flux sampling simulations (2013).

[68] R. J. Allen, D. Frenkel, and P. R. ten Wolde, Forward flux sampling-type schemes for simulating rare events: Efficiency analysis, *The Journal of Chemical Physics*, **124**, 194111 (2006).

[69] R. J. Allen, C. Valeriani, and P. R. ten Wolde, Forward flux sampling for rare event simulations, *Journal of Physics: Condensed Matter*, **21**, 463102 (2009).

[70] A. J. Liu and S. R. Nagel, Jamming is not just cool any more, *Nature*, **396**, 21–22 (1998).

[71] C. Patrick Royall, S. R. Williams, T. Ohtsuka, and H. Tanaka, Direct observation of a local structural mechanism for dynamic arrest, *Nat Mater*, **7**, 556–561 (2008).

[72] M. Tsamados, A. Tanguy, C. Goldenberg, and J. L. Barrat, Local elasticity map and plasticity in a model Lennard-Jones glass, *Physical Review E*, **80**, 026112 (2009).

[73] M. L. Manning and A. J. Liu, Vibrational Modes Identify Soft Spots in a Sheared Disordered Packing, *Physical Review Letters*, **107**, 108302+ (2011).

[74] R. L. Jack, A. J. Dunleavy, and C. P. Royall, Information-Theoretic Measurements of Coupling between Structure and Dynamics in Glass Formers, *Physical Review Letters*, **113** (2014).

[75] E. . D. Cubuk, S. . S. Schoenholz, J. . M. Rieser, B. . D. Malone, J. Rottler, D. . J. Durian, E. Kaxiras, and A. . J. Liu, Identifying Structural Flow Defects in Disordered Solids Using Machine-Learning Methods, *Physical Review Letters*, **114**, 108001–1–108001–5 (2015).

[76] D. Turnbull and M. H. Cohen, Freevolume model of the amorphous phase: Glass transition, *The Journal of Chemical Physics*, **34**, 120–125 (1961).

[77] L. Berthier, G. Biroli, J.-P. Bouchaud, L. Cipelletti, and W. van Saarloos, *Dynamical Heterogeneities in Glasses, Colloids, and Granular Media* (Oxford University Press) (2011), ISBN 9780199691470.

[78] M. Maiti and S. Sastry, Free volume distribution of nearly jammed hard sphere packings (2013).

[79] R. K. Shah, H. C. Shum, A. C. Rowat, D. Lee, J. J. Agresti, A. S. Utada, L.-Y. Chu, J.-W. Kim, A. Fernandez-Nieves, C. J. Martinez, and D. A. Weitz, Designer emulsions using microfluidics, *Materials Today*, **11**, 18–27 (2008).

[80] R. D. Cook, *Concepts and Applications of Finite Element Analysis* (Wiley, John) (2001).

[81] M. Lundberg, K. Krishan, N. Xu, C. S. O'Hern, and M. Dennin, Reversible plastic events in amorphous materials., *Physical review. E, Statistical, nonlinear, and soft matter physics*, **77**, 041505+ (2008).

[82] D. Chen, K. W. Desmond, and E. R. Weeks, Topological rearrangements and stress fluctuations in quasi-two-dimensional hopper flow of emulsions, *Soft Matter*, **8**, 10486–10492 (2012).